AE - 5100: Final Report

Finite Element Analysis of an Electrospray Emitter Chip

Nathaniel Allwine

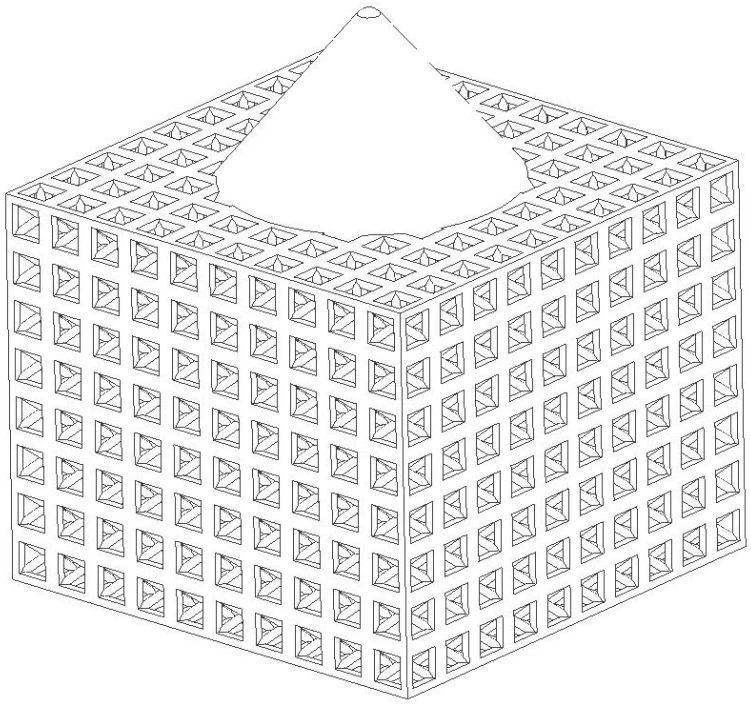

7th December 2022

Contents

Abstract

Single emitter porous borosilicate models were developed with four different internal porous structures. These models were subjected to launch loads intended to verify structural integrity of cube satellite structures. Those loads are 30G quasi-static loads in each axes and random vibration loads conforming to NASA's General Environmental Verification Standard (GEVS-STD-7000). It was found that all four models passed Coulomb-Mohr failure criteria and have large factors of safety.

1 Introduction

Electric propulsion (EP) devices have been gaining popularity and are being implemented into an increasing number of space missions. Electric propulsion devices utilize on board power systems to accelerate a propellant and produce thrust. This is different to the conventional chemical propulsion since chemical engines use chemical reactions to combust a propellant and expel high velocity hot gas to produce thrust. Electric propulsion devices have very low thrust compared to chemical rockets, however, have significantly higher specific impulse. With their high performance and scalability, CubeSats are now employing EP devices for attitude control and executting complex missions. With recent technological improvements, EP devices have low mass, smaller space requirements, and provide better efficiency than their chemical counterparts. They have become a prime candidates for plenty of space missions.[1][2]

One such EP device that has been showing promising results is an electrospray thruster (EST). Electrosprays provide a large electrical potential difference between an extractor grid and a liquid propellant. The strong electric field will produce large electrostatic forces that overcome the surface tension of the liquid and extract ions and droplets from the propellant.

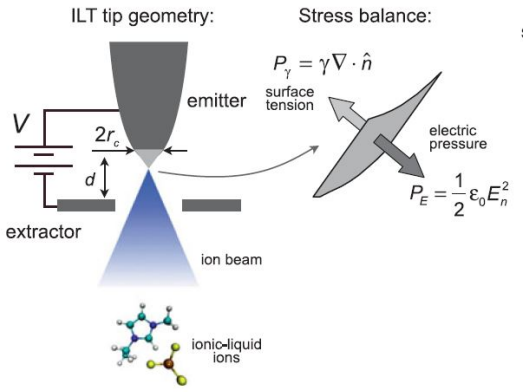

Figure 1: Emitter Geometry and Force Balance [2]

Electrosprays use a porous media to passively feed propellant close to the extractor grid. This has the added benefit of removing complex feed systems found in other types of propulsion systems. The porous media emitter will have extremely small cones to transport propellant as close as possible to the extractor grid and amplify the electric field.

2 Background

Electrosprays generally use ionic liquids for propellant. Ionic liquids are room temperature molten salts that are composed of both negatively and positively charged of ions. A thruster will emit one charge of ions depending on the orientation of the electric potential. Since only one charge of ion is being expelled at a time, the other charge ion or counterions will accumulate on the emitter tip. Counterion buildup can results in electrochemical reactions occurring on the emitter, which degrades the emitter and could prevent firing of the thruster. Although the electrical bias will be alternated at a certain frequency, counterion buildup can still occur. To further eliminate this risk, current thrusters use machined porous borosilicate glass, which has a high chemical resistance, for the emitter chips.

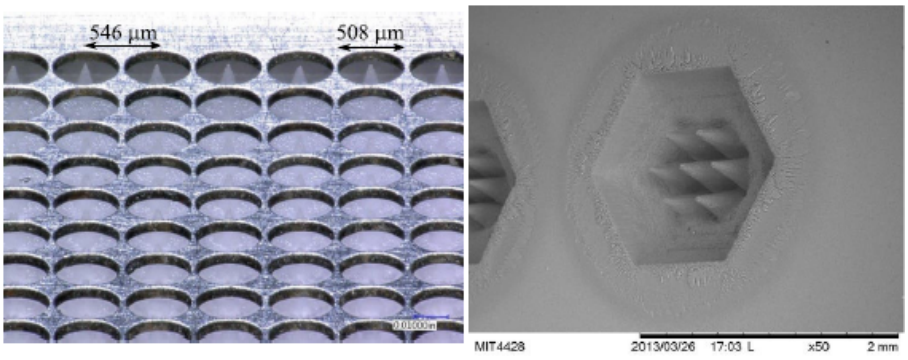

Figure 2: (Left) Airforce Electrospray Thruster 2 (AFET-2) emitter grid [3]. (Right) Borosilicate glass ablated using a nanosecond laser. [4]

3 Motivation

Western Aerospace Launch Initiative (WALI) at WMU is developing a cube satellite that will include an electrospray thruster as the main technological demonstration and is involved with the main mission success criteria. WALI has recently started a partnership with Dr. Paulo Lozano's Space Propulsion Laboratory at Massachusetts Institute of Technology to use their ion Electrospray Propulsion System (iEPS) for the mission.

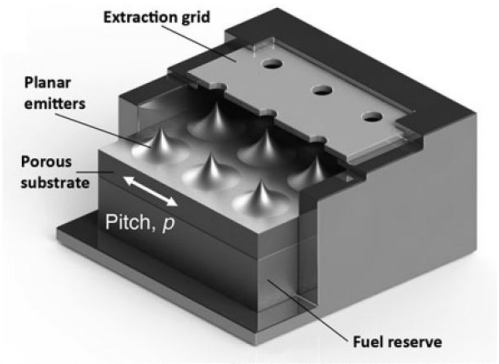

Figure 3: Schematic of iEPS Thruster [4]

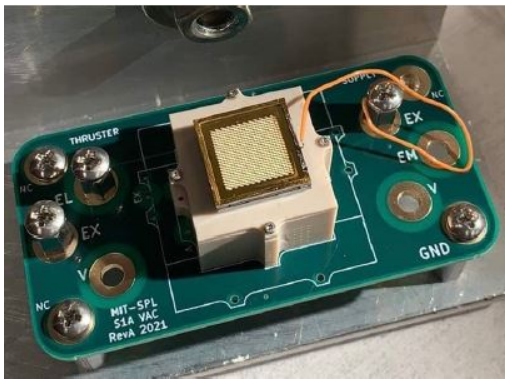

Figure 4: iEPS Thruster on Breakout Board for Testing [4]

With the EST being a crucial component for mission success, having limited flight heritage, and using a non-conventional material, there have been significant fears that the porous borosilicate emitter chip might break due to the severe launch environment. This project aims at investigating the structural rigidity of an electrospray emitter chip.

4 Project Definition and Scope

This project seeks to model a porous borosilicate electrospray emitter in a finite element software and subject the model to load cases used to validate satellite structure models. The load cases include static 30 G loads in all three axes as well as random vibration conforming to NASA's General Environmental Verification Standard (GEVS-STD-7000). This work will complete the following objectives:

- Complete a porous borosilicate electrospray emitter finite element model
- Perform 30G static load cases in all three axes
- Perform random vibration load using NASA's GEVS-STD-7000

Frequency (Hz)	ASD Level (g^2/Hz)	
	Qualification	Acceptance
20	0.026	0.013
20-50	+6 dB/oct	+6 dB/oct
50-800	0.16	0.08
800-2000	-6 dB/oct	-6 dB/oct
2000	0.026	0.013
Overall	14.1 G_{rms}	10.0 G_{rms}

The acceleration spectral density level may be reduced for components weighing more than 22.7-kg (50 lb) according to:

	Weight in kg	Weight in lb	
dB reduction	= 10 log(W/22.7)	10 log(W/50)	
$ASD_{(50\text{-}800\ Hz)}$	= 0.16•(22.7/W)	0.16•(50/W)	for protoflight
$ASD_{(50\text{-}800\ Hz)}$	= 0.08•(22.7/W)	0.08•(50/W)	for acceptance

Where W = component weight.

The slopes shall be maintained at + and - 6dB/oct for components weighing up to 59-kg (130-lb). Above that weight, the slopes shall be adjusted to maintain an ASD level of 0.01 g^2/Hz at 20 and 2000 Hz.

For components weighing over 182-kg (400-lb), the test specification will be maintained at the level for 182-kg (400 pounds).

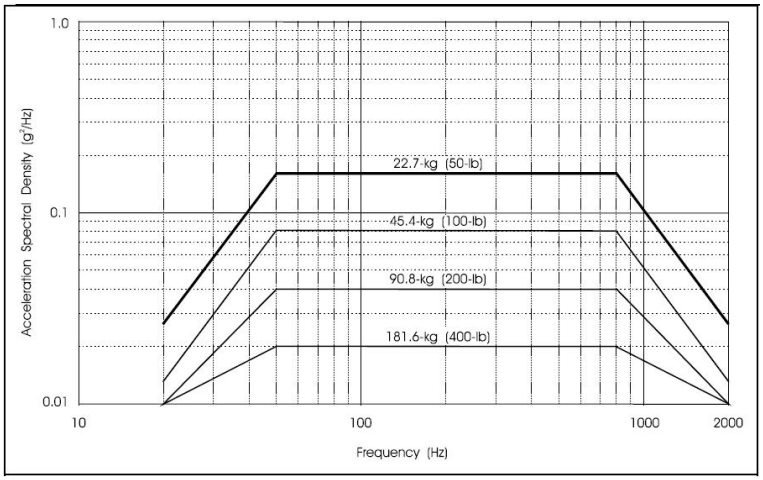

Figure 5: NASA's GEVS-STD-700 Random Vibration Criteria [5]

5 Methods

The emitter chip modeled will be based off the iEPS design. The emitter chips used have 480 tips that are on average 175 μm tall [6][7]. The emitter tips were manufactured from 1x1 cm porous borosilicate and the initial material height was 1 mm before machining [7][8]. The tip curvature has a radii of around 15 μm with a pitch, or tip spacing, of 450 μm [7].

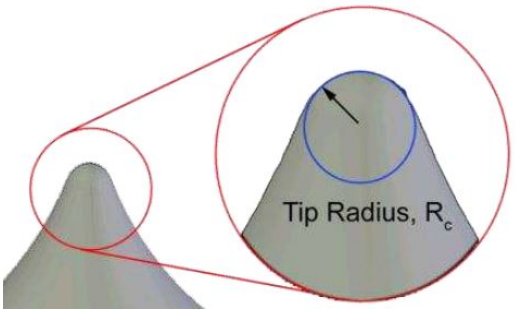

Figure 6: Emitter Tip Radius [8]

The final porosity of the model, which is defined as the ratio of void volume to total volume, $\phi = \frac{V_V}{V_T}$, should be between 20 and 50% [8]. Additionally pore size can range from 1-10 μm within the borosilicate [7]. Initial attempts were made to develop an entire emitter chip model, however due to the shear amount of geometry needed to produce this model, this was not a reasonable approach. If the voids were modeled as perfect spheres with radius of 5 μm the individual void volumes are calculated.

$$\frac{4}{3}\pi r^3 = \frac{4}{3}\pi(5)^3 = 523.6\mu m^3 \tag{1}$$

Then assuming a porosity of 50% the amount of sphere necessary to model are calculated.

$$0.5 = \frac{523.6 \times n}{10000 \times 10000 \times 1000} \therefore n = 9.549e7 \text{ Spheres} \tag{2}$$

As can be seen, the amount of spheres necessary would require a significant amount of compute power just to model. Therefore, a scaled down approach was used for this project.

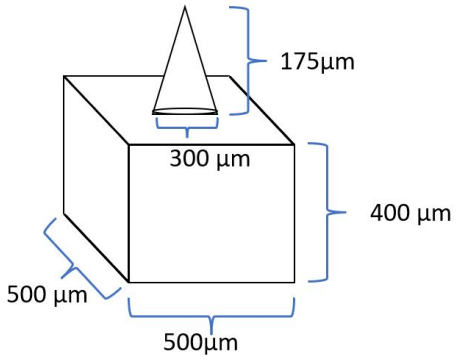

Figure 7: Scaled Down Geometry

As can be seen in figure (7), the base of the emitter was modeled to be 500 μm by 500 μm by 400 μm with an emitter tip geometry having a base radius of 150 μm a height of

175 μm and a tip radius of 15 μm. Porosity for this geometry was produced with unit cube structures developed by Mehboob et al [9].

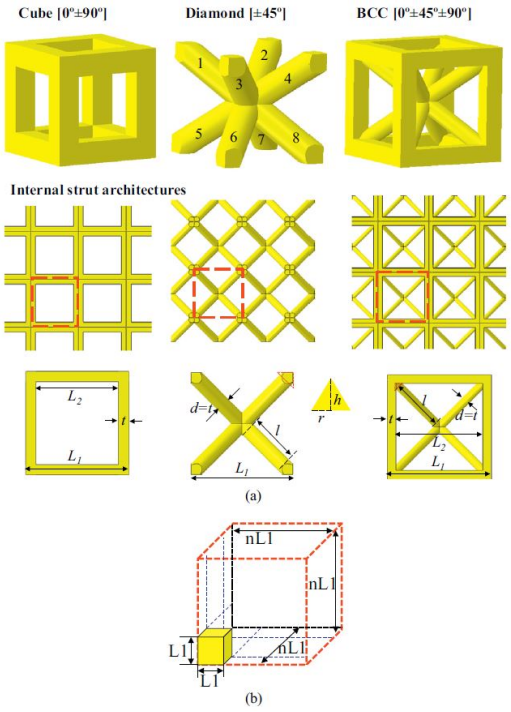

Figure 8: Unit Cube Geometry [9]

The unit cubes have dimensions of 50μm by 50 μm by 50μm. Additionally, a spherical unit cube was developed which is similar to the cube geometry except with a sphere at the center of the unit cube. The internal geometric dimensions of the unit cubes could be solved for by defining a set porosity. This porosity was set to 0.6 which is more porous than normal electrospray emitters in order to add some contingency to the final results. Based on the equations from Mehboob et al., the following equations were solved to determine internal dimensions [9].

- Cube Thickness

$$V_{cube} = L_1^3 - L_2^3 - 6(L_2^2 \times t) \tag{3}$$

$$0.6 = \frac{50^3 - (50^3 - (50 - 2 \times t)^3 - (6 \times ((50 - 2 \times t)^2 \times t)))}{50^3} \therefore t = 10.8233\mu m \tag{4}$$

- Sphere Radius

$$0.6 = \frac{\frac{4}{3}\pi r^3}{50^3} \therefore r = 26.1612\mu m \tag{5}$$

- Diamond Thickness

$$V_{cone} = 1/3 \times \pi(t/2)^2 t \tag{6}$$

$$l = \sqrt{3}/2 \times L_1 - t \tag{7}$$

$$V_{cyl} = \pi(t/2)^2 l \tag{8}$$

$$V_{dia} = (2 \times V_{cone} + V_{cyl}) \times 8 \tag{9}$$

$$0.6 = \frac{50^3 - (2 \times (1/3 \times \pi \times (0.5 \times t)^2 \times 0.35t) + (\pi \times (0.5 \times t)^2 \times (\sqrt{3}/2 \times 50 - t))) \times 8}{50^3}$$

$$\therefore t = 17.3396\mu m$$

- Body Centered Cubic (BCC) Thickness

$$V_{BCC} = (2 \times V_{cone} + V_{cyl}) \times 8 + V_{cube} \tag{10}$$

$$0.6 = (50^3 - ((2 \times (1/3 \times \pi \times (0.5 \times t)^2 \times 0.35t) + (\pi \times (0.5 \times t)^2 \times (\sqrt{3}/2 \times 50 - t))) \times 8 + (50^3 - (50 - 2 \times t)^3 - (6 \times ((50 - 2 \times t)^2 \times t))50^3))) \times 1/50^3 \therefore t = 8.39395\mu m$$

The models were produced in AutoDesk Inventor.

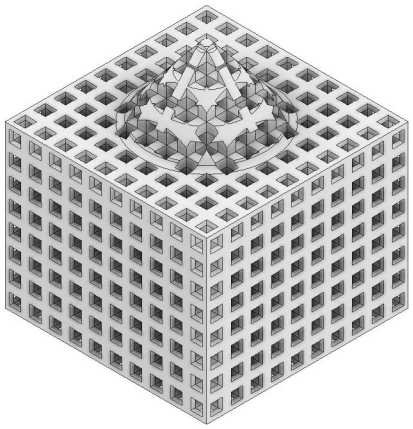

Figure 9: Cube Model

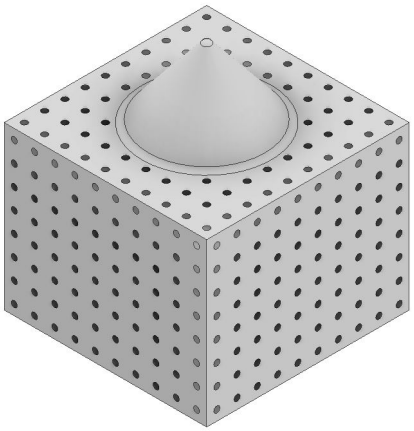

Figure 10: Sphere Model

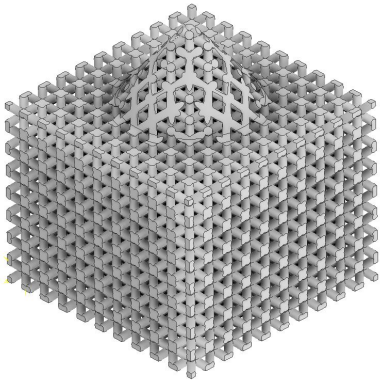

Figure 11: Diamond Model

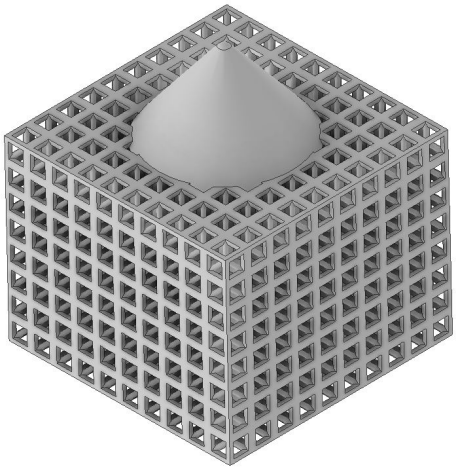

Figure 12: BCC Model

These models were meshed within GMSH, an open source meshing tool.

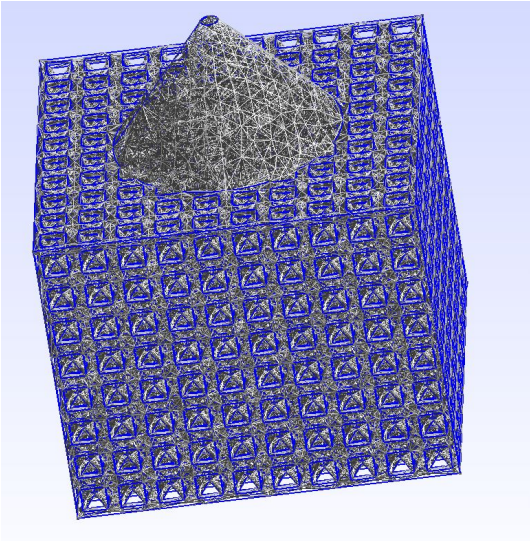

Figure 13: Example of Mesh Within GMSH

The mesh properties can be seen in Tabel (1) for each of the models.

	Nodes	Triangle Elements	Tetrahedral Elements	Total Elements
Cube Mesh	19,976	47,370	59,800	107,170
Sphere Mesh	205,514	360,318	753,875	1,114,193
Diamond Mesh	148,998	308,732	474,544	783,276
BCC Mesh	205,488	431,436	668,687	1,100,123

Table 1: Mesh Properties for Each Model

These mesh models would then be imported into Abaqus to perform the load cases. The mechanical properties used for structural analysis are summarized in Table (2).

Property	Value
ρ (g/cm3)	2.23 [10]
E (GPa)	64 [10]
v	0.2 [11]
Ultimate Yield Strength (MPa)	10.1 [12]
Compressive Strength (MPa)	2000 [11]

Figure 14: Borosilicate Mechanical Properties

Based on the exploded CAD model for the iEPS unit, it was assumed that the insulating layer corner pieces enveloped the corners of the emitter chip and would therefore keep them fixed. For this reason, the boundary conditions for all the model cases were set to have fixed nodes on the edges at the corners.

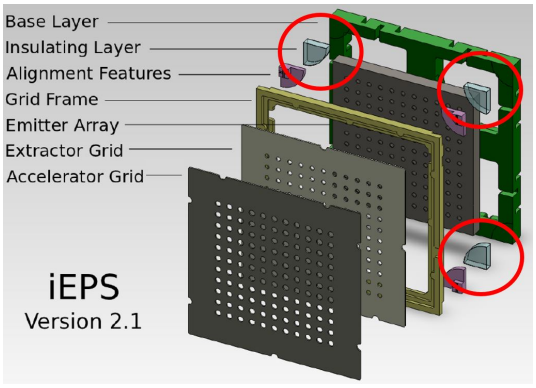

Figure 15: Exploded CAD Model of iEPS [6]

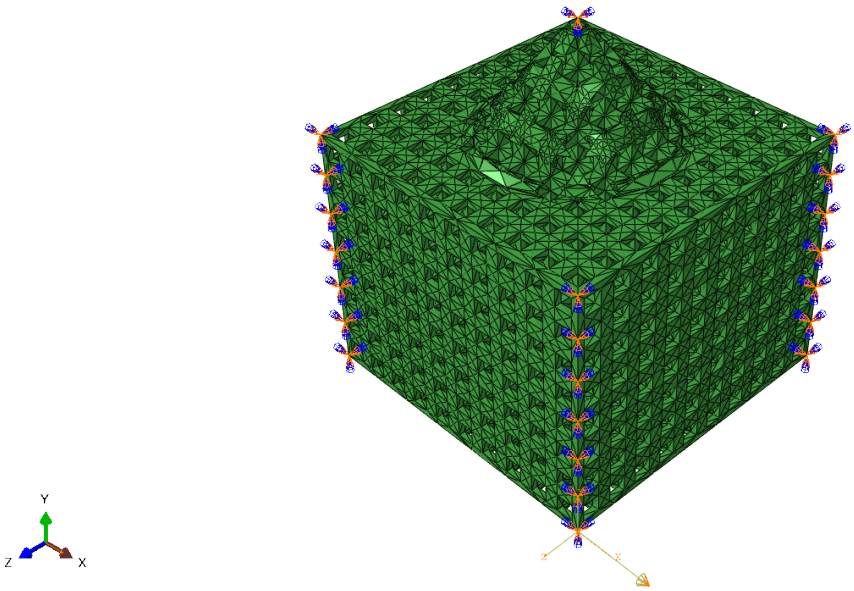

Figure 16: Fixed Boundary Condition for Cube Model

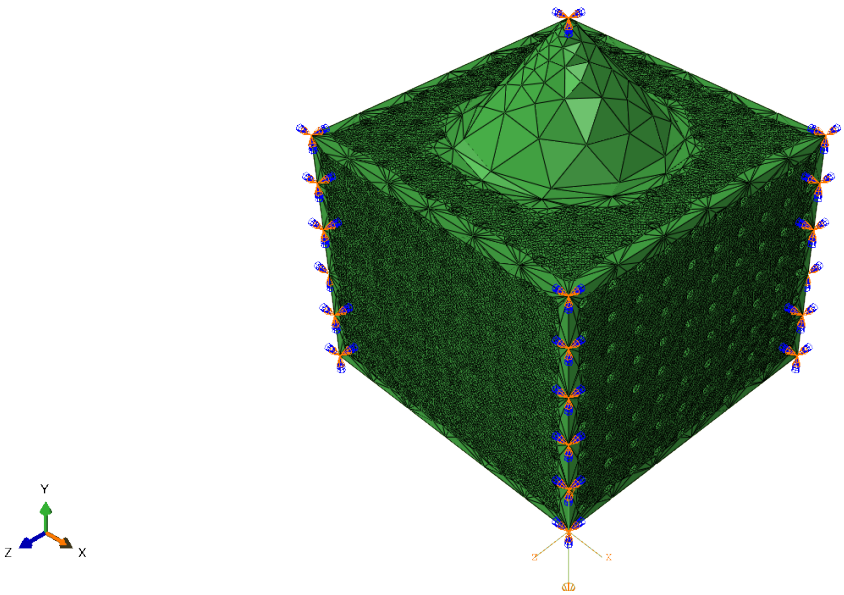

Figure 17: Fixed Boundary Condition for Sphere Model

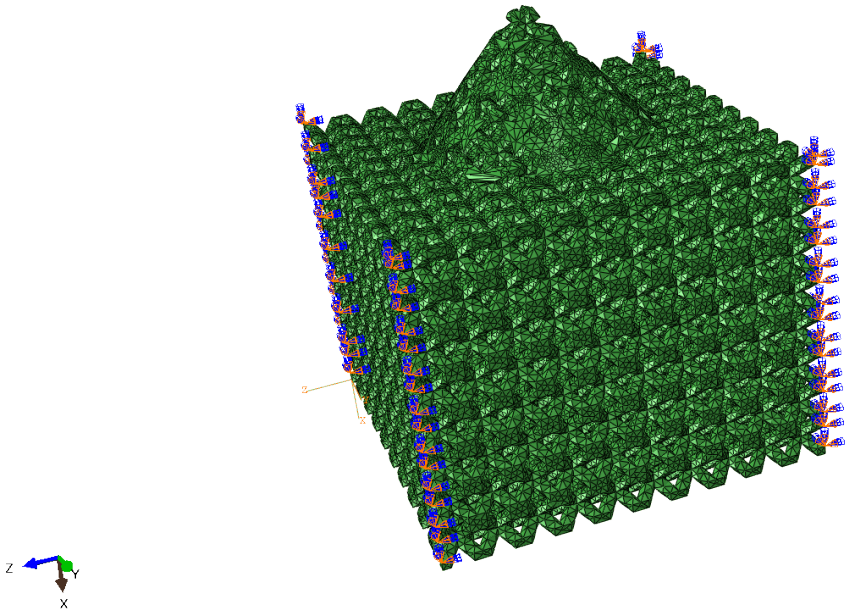

Figure 18: Fixed Boundary Condition for Diamond Model

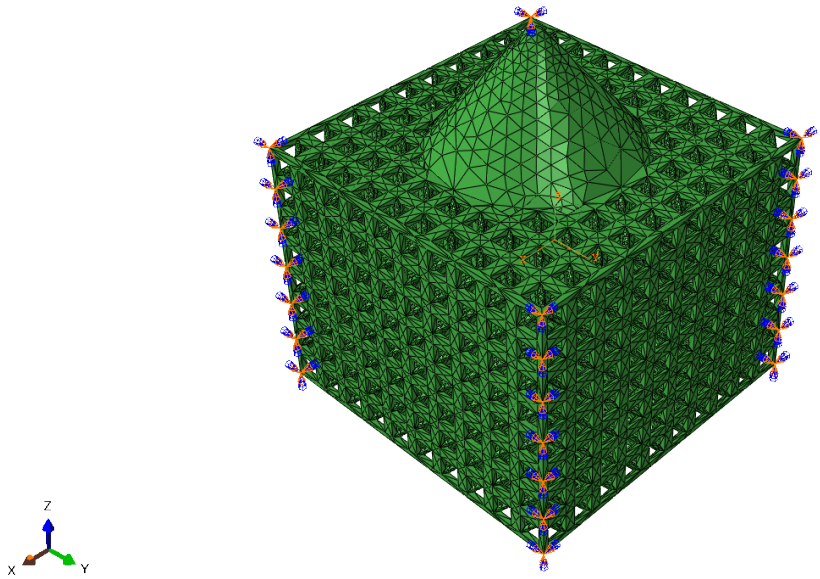

Figure 19: Fixed Boundary Condition for BCC Model

Additionally, the load cases were defined the same for each model for comparison. For

clarity Figure (20) shows the cartesian frame used to define the loads throughout this report. It should be noted that the positive Z axis in toward the cones tip, when the negative Z axis is toward the bottom. Additionally, there is symmetry such that the positive and negative X and Y axis would be identical, therefore only the positive X load cases were simulated.

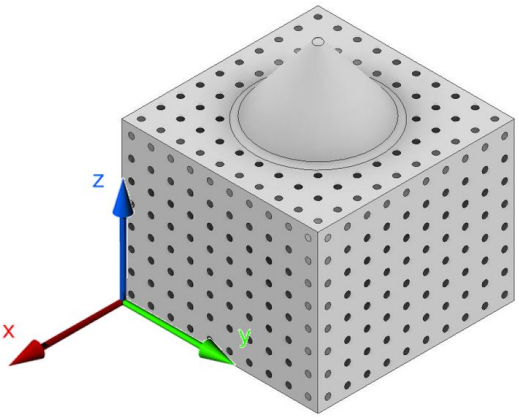

Figure 20: Coordinate Definition for Loads

6 Results and Interpretation

The models would be ran through Abaqus and results were post processed. An example of Abaqus results can be seen in Figure (21) with the entirety of the results available in the appendix.

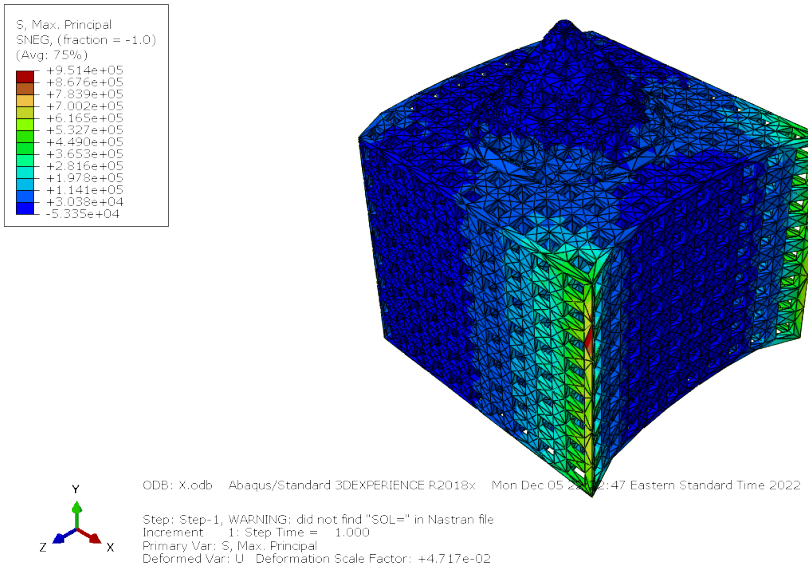

Figure 21: Max Principal Stress Results from 30 G Load in X Direction on Cube Emitter Model

The Coulomb-Mohr failure criteria was used to determine if the models would fail to the loads. This was selected because borosilicate glass is a brittle material. The following equations were used to define failure and factor of safety (FOS) for the static G loads:

$$\frac{\sigma_1}{UTS} - \frac{\sigma_3}{UCS} \leq 1[13] \tag{11}$$

$$FOS = \frac{1}{\frac{\sigma_1}{UTS} - \frac{\sigma_3}{UCS}}[13] \tag{12}$$

Where σ_1 is the maximum principle stress, σ_2 is the minimum principal stress, UTS is the ultimate tensile strength, and UCS is ultimate compressive strength. Additionally for the random vibration, the following failure criteria equations were used:

$$RMises < UTS \tag{13}$$

$$FOS = \frac{UTS}{RMises} \tag{14}$$

Where RMises is the root mean squared Von Mises stress. The following results were found for each geometry.

Load	Max σ1	Max σ3	Max Von Mises
30G in X	9.51E+05	-7.09E+05	7.06E+05
30G in Z+	1.49E+06	-1.49E+06	9.67E+05
30G in Z-	1.49E+06	-1.49E+06	9.67E+05
Vibe	N/A	N/A	2.073E+05

Table 2: Cube Model Results

Load	Failure Criteria [Pass/Fail]	Factor of Safety
30G in X	PASS	8.857
30G in Z+	PASS	5.661
30G in Z-	PASS	5.66
Vibe	PASS	4052.098

Table 3: Cube Model Conclusion

Mode	Frequency [Hz]
1	1357.5
2	1664.3
3	1664.9
4	1738.8
5	1739

Table 4: Cube Model Natural Frequencies

Load	Max σ1 [Pa]	Max σ3 [Pa]	Max Von Mises [Pa]
30G in X	6.39E+03	-2.36E+04	1.82E+04
30G in Z+	9.26E+03	-1.15E+04	1.43E+04
30G in Z-	1.15E+04	-9.26E+03	1.43E+04
Vibe	N/A	N/A	1.87E+04

Table 5: Sphere Model Results

Load	Failure Criteria [Pass/Fail]	Factor of Safety
30G in X	PASS	1334
30G in Z+	PASS	911
30G in Z-	PASS	731
Vibe	PASS	450

Table 6: Sphere Model Conclusion

Mode	Frequency [Hz]
1	1432.3
2	1541.6
3	1542.6
4	1664.4
5	1684
6	1684.2

Table 7: Sphere Model Natural Frequencies

Load	Max σ1 [Pa]	Max σ3 [Pa]	Max Von Mises [Pa]
30G in X	1.66E+04	-1.77E+04	2.30E+04
30G in Z+	1.24E+04	-2.59E+04	2.14E+04
30G in Z-	2.59E+04	-1.24E+04	2.14E+04
Vibe	N/A	N/A	3.03E+04

Table 8: Diamond Model Results

Load	Failure Criteria [Pass/Fail]	Factor of Safety
30G in X	PASS	507
30G in Z+	PASS	684
30G in Z-	PASS	325
Vibe	PASS	277

Table 9: Diamond Model Conclusion

Mode	Frequency [Hz]
1	1127.7
2	1228.3
3	1233.8
4	1283.4
5	1288
6	1586.8

Table 10: Diamond Model Natural Frequencies

Load	Max σ1 [Pa]	Max σ3 [Pa]	Max Von Mises [Pa]
30G in X	3.50E+04	-3.14E+04	2.89E+04
30G in Z+	3.04E+04	-1.96E+04	3.63E+04
30G in Z-	1.96E+04	-3.04E+04	3.63E+04
Vibe	N/A	N/A	2.89E+04

Table 11: BCC Model Results

Load	Failure Criteria [Pass/Fail]	Factor of Safety
30G in X	PASS	240
30G in Z+	PASS	277
30G in Z-	PASS	432
Vibe	PASS	262

Table 12: BCC Model Conclusion

Mode	Frequency [Hz]
1	1249.9
2	1482.7
3	1482.9
4	1524.7
5	1526.2

Table 13: BCC Model Natural Frequencies

7 Discussion

For each model of the porous structure, each failure criteria was passed with a large factor of safety, therefore providing evidence that a porous borosilicate emitter chip would survive the launch conditions. That being said, the entire emitter was not completely modeled so the validity of the results could be questioned. Additionally, the porous structure was modeled with lattice unit cube structures which isn't perfectly representative of the random pore distribution within actual porous borosilicate. Impact forces were also not investigated which is large form of failure for brittle materials. More complex models with the entire electrospray thruster with contacts would probably be a significant improvement to the boundary conditions presented in this report. Although not in the scope of this project, off axis load where not subjected onto the model but could be valuable information to ensure survivability of the emitter. Significant vibrational and static load testing should still be completed in order to verify the computational model results.

References

[1] Lemmer, K. (2017). Propulsion for CubeSats. Acta Astronautica, 134, 231–243. https://doi.org/10.1016/j.actaastro.2017.01.048

[2] Lozano, P. C., Wardle, B. L., Moloney, P., & Rawal, S. (2015). Nanoengineered thrusters for the next giant leap in space exploration. MRS Bulletin, 40(10), 842–849. https://doi.org/10.1557/mrs.2015.226

[3] Natisin, M. R., Zamora, H. L., Holley, Z. A., Ivan Arnold, N., McGehee, W. A., Holmes, M. R., & Eckhardt, D. (2021). Efficiency mechanisms in porous-media electrospray thrusters. Journal of Propulsion and Power, 37(5), 650–659. https://doi.org/10.2514/1.b38160

[4] Coffman, C. S., Perna, L., Li, H., & Lozano, P. C. (2013). On the manufacturing and emission characteristics of dielectric electrospray sources. 49th AIAA/ASME/SAE/ASEE Joint Propulsion Conference. https://doi.org/10.2514/6.2013-4035

[5] GSFC-STD-7000A The General Environmental verification standard for GSFC Flight Programs and Projects. http://standards.gsfc.nasa.gov

[6] Perna, Louis, et al. "Progress toward Demonstration of Remote, Autonomous Attitude Control of a CubeSat Using Ion Electrospray Propulsion Systems." 48th AIAA/ASME/SAE/ASEE Joint Propulsion Conference amp; Exhibit, 2012, https://doi.org/10.2514/6.2012-4289.

[7] Krejci, David, et al. "Emission Characteristics of Passively Fed Electrospray Microthrusters with Propellant Reservoirs." Journal of Spacecraft and Rockets, vol. 54, no. 2, 2017, pp. 447–458., https://doi.org/10.2514/1.a33531.

[8] Courtney, D., "Ionic Liquid Ion Source Emitter Arrays Fabricated on Bulk Porous Substrates for Spacecraft Propulsion," Doctor of Philosophy Thesis, Massachusetts Institute of Technology, Cambridge, MA, (2011)

[9] Mehboob, Hassan, et al. "Finite Element Modelling and Characterization of 3D Cellular Microstructures for the Design of a Cementless Biomimetic Porous Hip Stem." Materials Design, vol. 149, 2018, pp. 101–112., https://doi.org/10.1016/j.matdes.2018.04.002.

[10] Bouras, N., et al. "Thermal and Mechanical Characterization of Borosilicate Glass." Physics Procedia, vol. 2, no. 3, 2009, pp. 1135–1140., https://doi.org/10.1016/j.phpro.2009.11.074.

[11] Chojnacki, John T., and Weinong W. Chen. "Mechanical Response of Borosilicate and Soda-Lime Glass under Dynamic Triaxial Compression." Journal of Dynamic Behavior of Materials, vol. 2, no. 2, 2016, pp. 251–258., https://doi.org/10.1007/s40870-016-0063-5.

[12] Lee, Kuo-Hao, et al. “Plasticity of Borosilicate Glasses under Uniaxial Tension.” Journal of the American Ceramic Society, vol. 103, no. 8, 2020, pp. 4295–4303., https://doi.org/10.1111/jace.17163.

[13] Less Boring Lectures. COULOMB-MOHR Failure Criterion Example in 2 Minutes! YouTube, YouTube, 15 Mar. 2021, https://www.youtube.com/watch?v=LYHGW8AIUDY. Accessed 6 Dec. 2022.

A Appendix

A.1 Cube Model

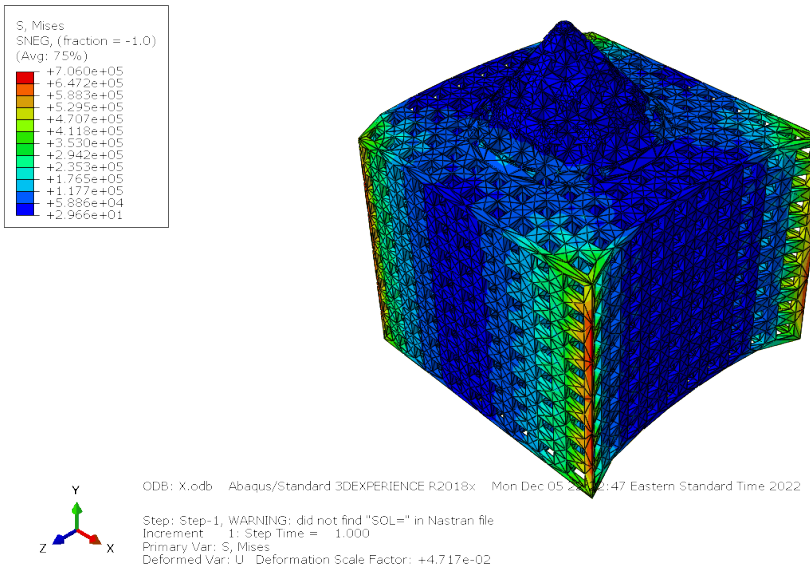

Figure 22: Von Mises Results from 30 G Load in X Direction on Cube Emitter Model

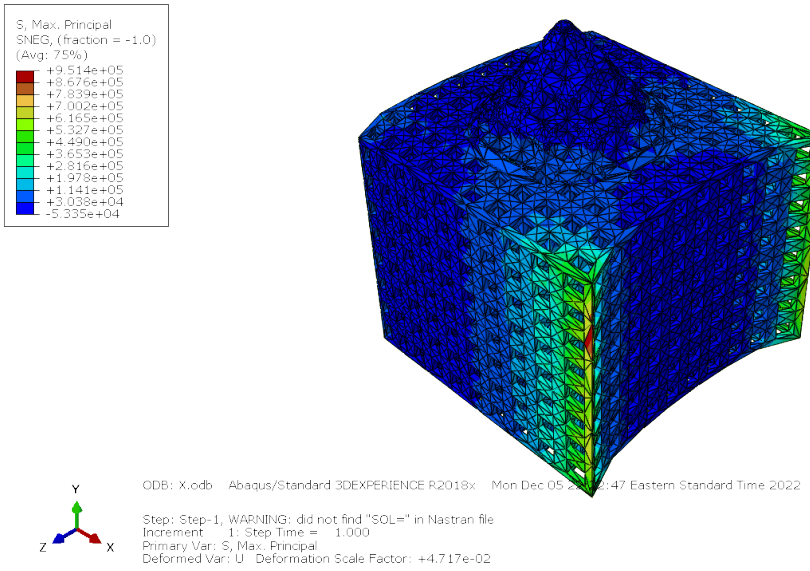

Figure 23: Max Principal Stress Results from 30 G Load in X Direction on Cube Emitter Model

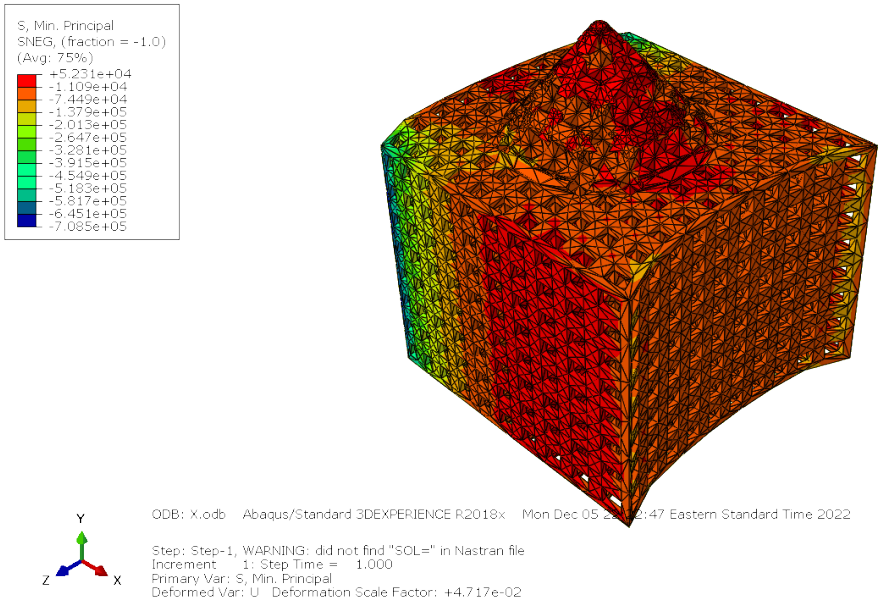

Figure 24: Min Principal Stress Results from 30 G Load in X Direction on Cube Emitter Model

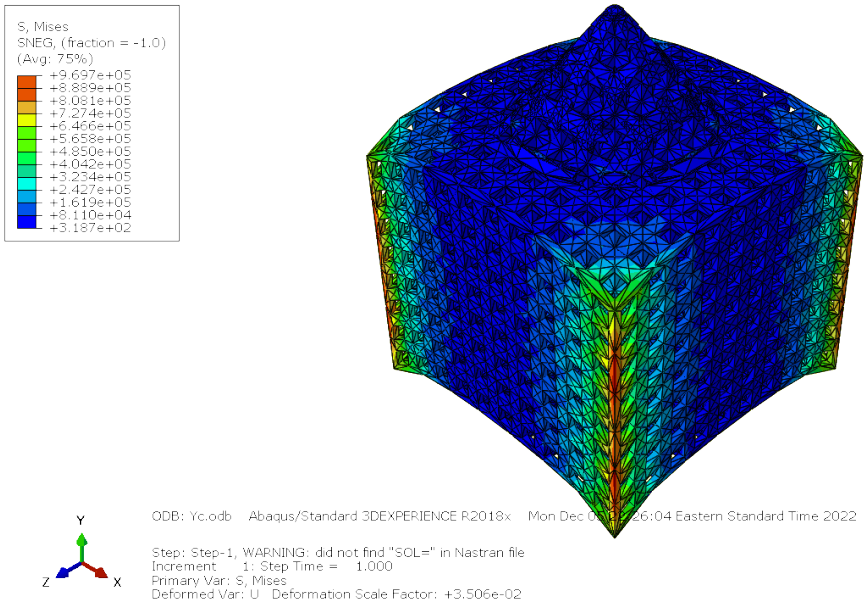

Figure 25: Von Mises Results from 30 G Load in +Z Direction on Cube Emitter Model

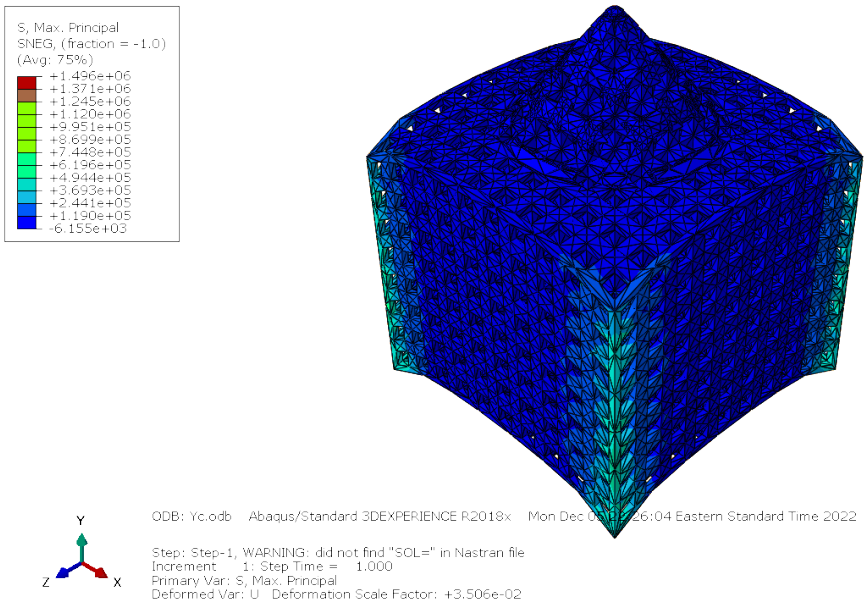

Figure 26: Max Principal Stress Results from 30 G Load in +Z Direction on Cube Emitter Model

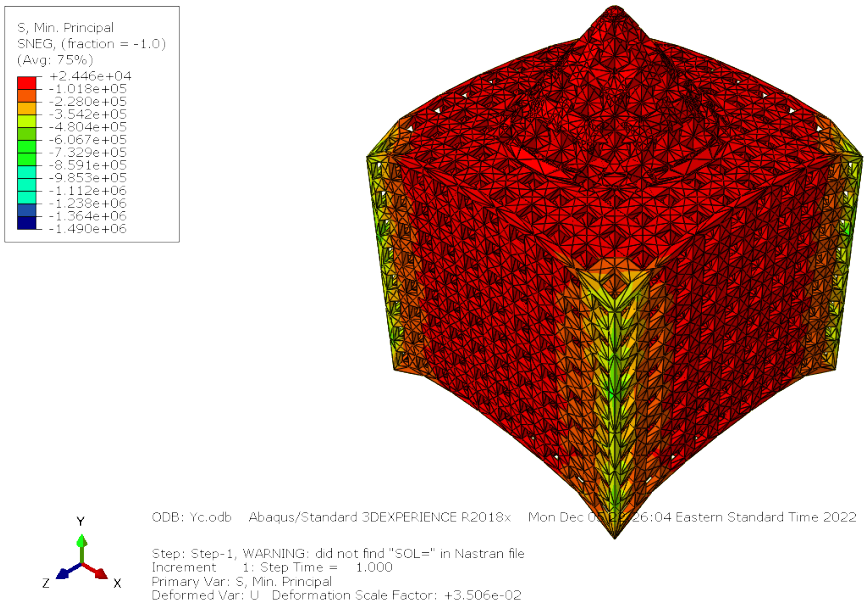

Figure 27: Min Principal Stress Results from 30 G Load in +Z Direction on Cube Emitter Model

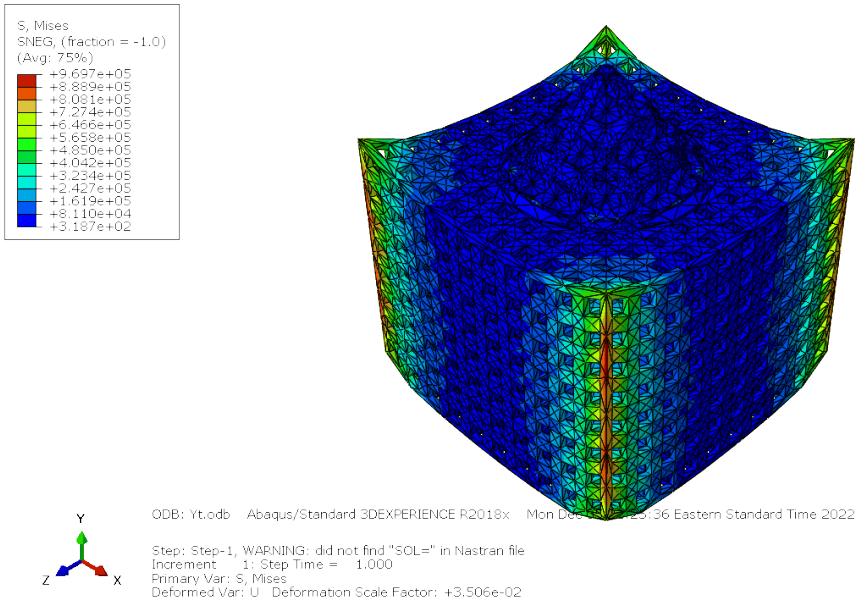

Figure 28: Von Mises Results from 30 G Load in -Z Direction on Cube Emitter Model

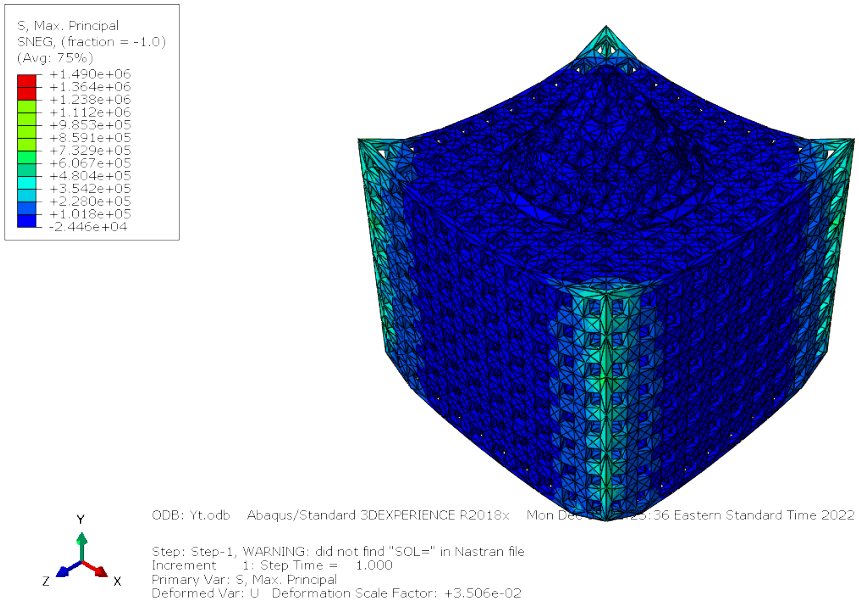

Figure 29: Max Principal Stress Results from 30 G Load in -Z Direction on Cube Emitter Model

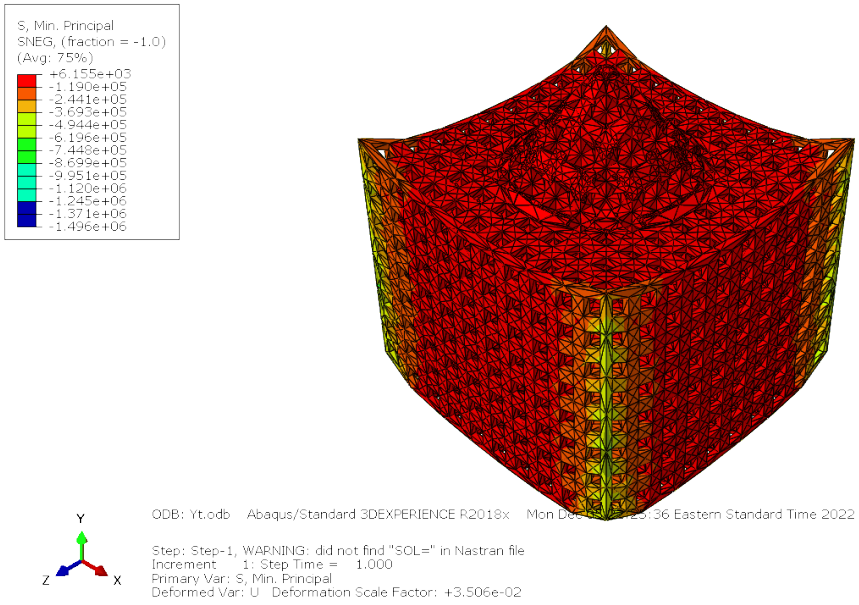

Figure 30: Min Principal Stress Results from 30 G Load in -Z Direction on Cube Emitter Model

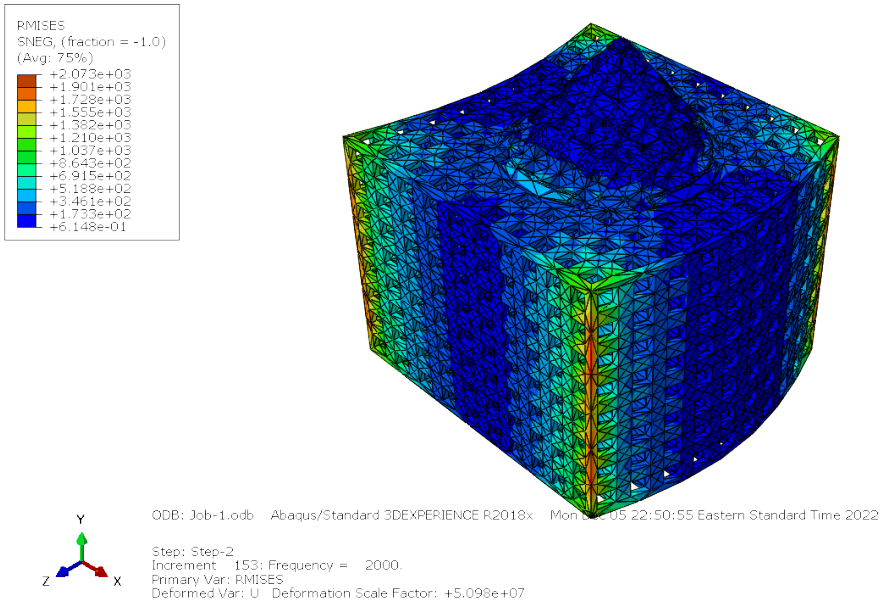

Figure 31: Root Mean Squared Von Mises Stress Results from Random Vibe on Cube Emitter Model

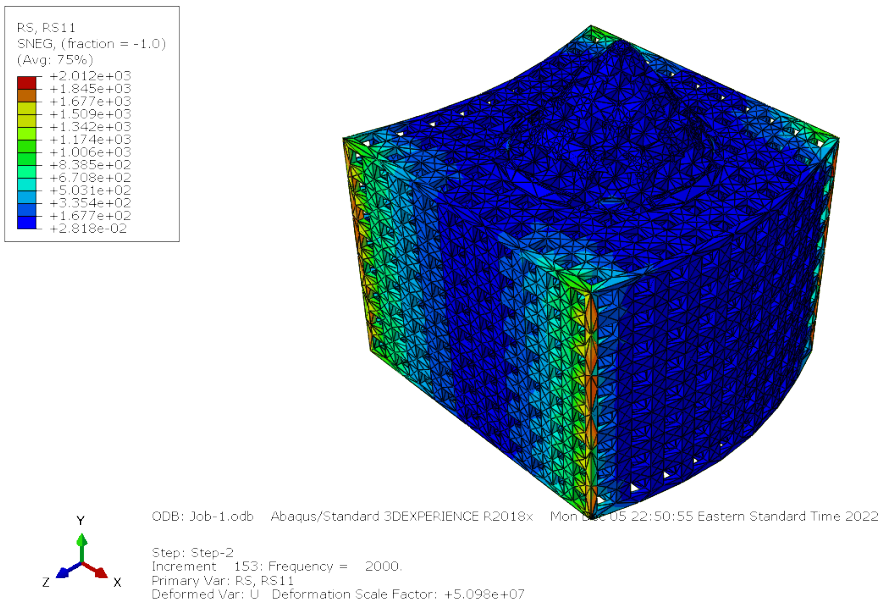

Figure 32: Root Mean Squared Stress Results from Random Vibe on Cube Emitter Model

A.2 Sphere Model

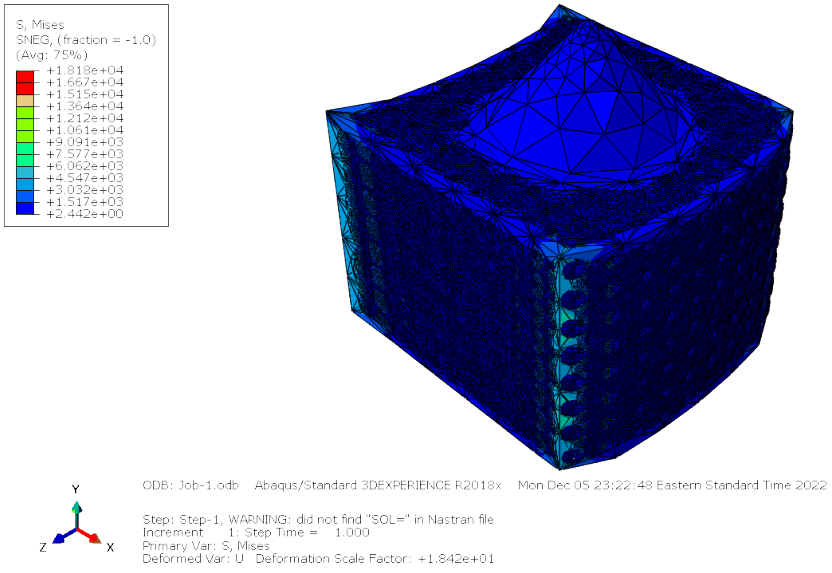

Figure 33: Von Mises Results from 30 G Load in X Direction on Sphere Emitter Model

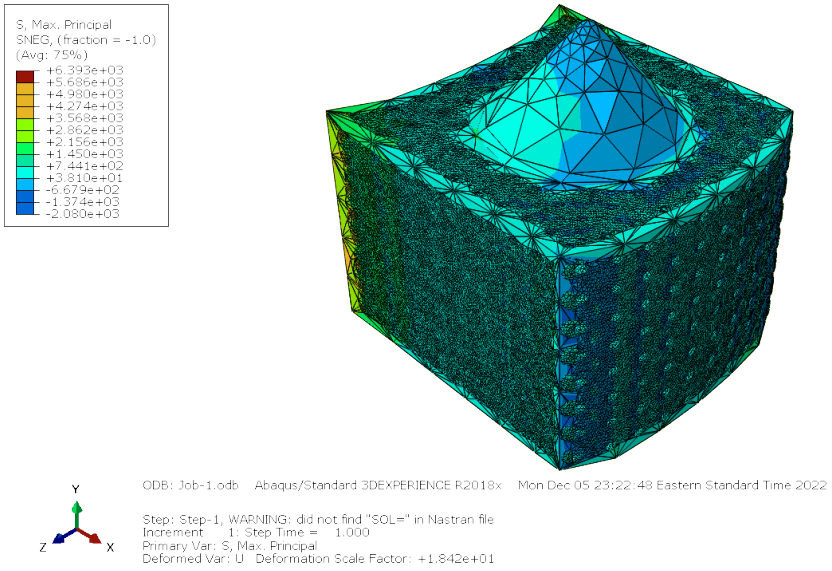

Figure 34: Max Principal Stress Results from 30 G Load in X Direction on Sphere Emitter Model

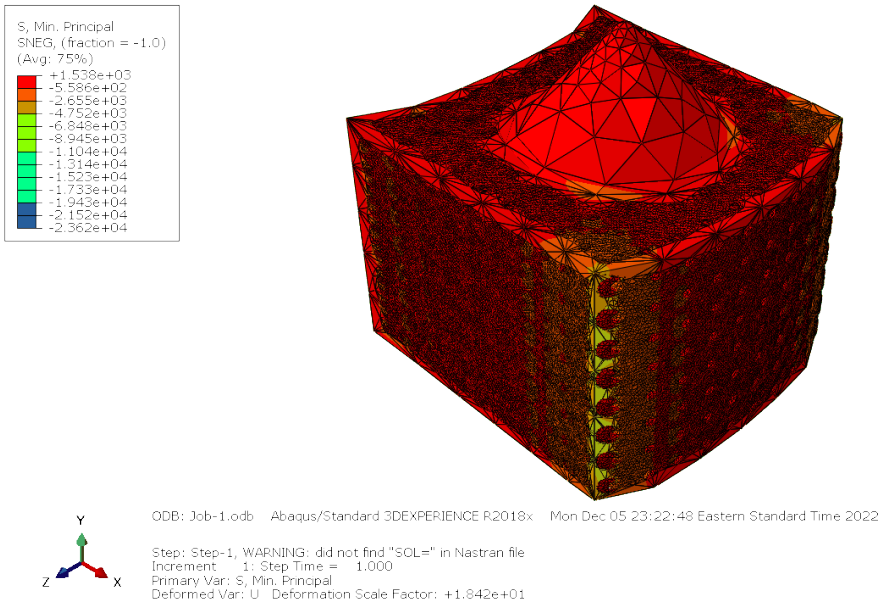

Figure 35: Min Principal Stress Results from 30 G Load in X Direction on Sphere Emitter Model

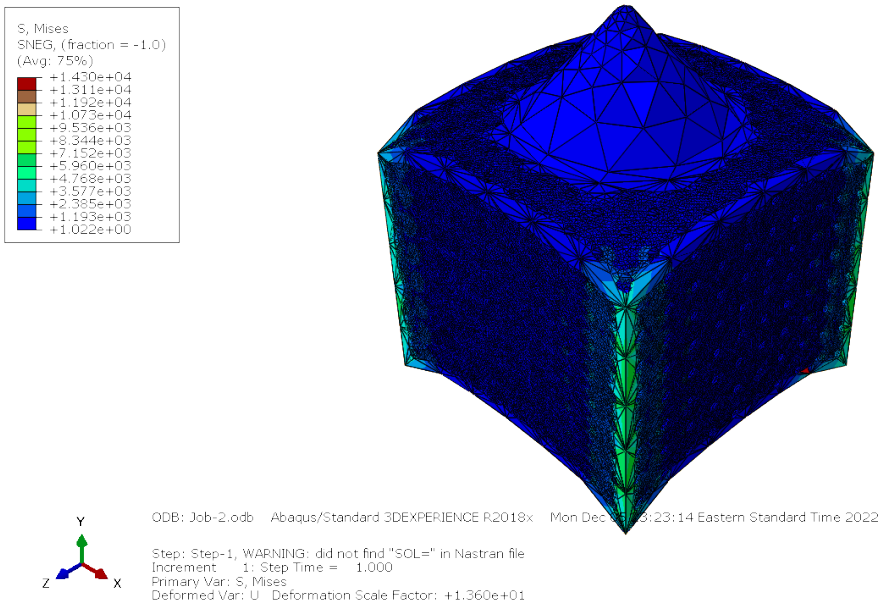

Figure 36: Von Mises Results from 30 G Load in +Z Direction on Sphere Emitter Model

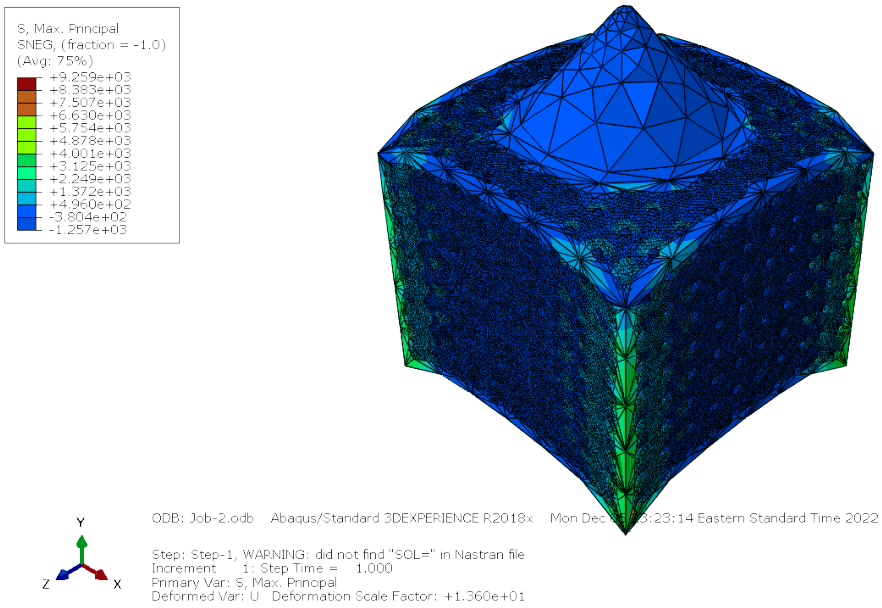

Figure 37: Max Principal Stress Results from 30 G Load in +Z Direction on Sphere Emitter Model

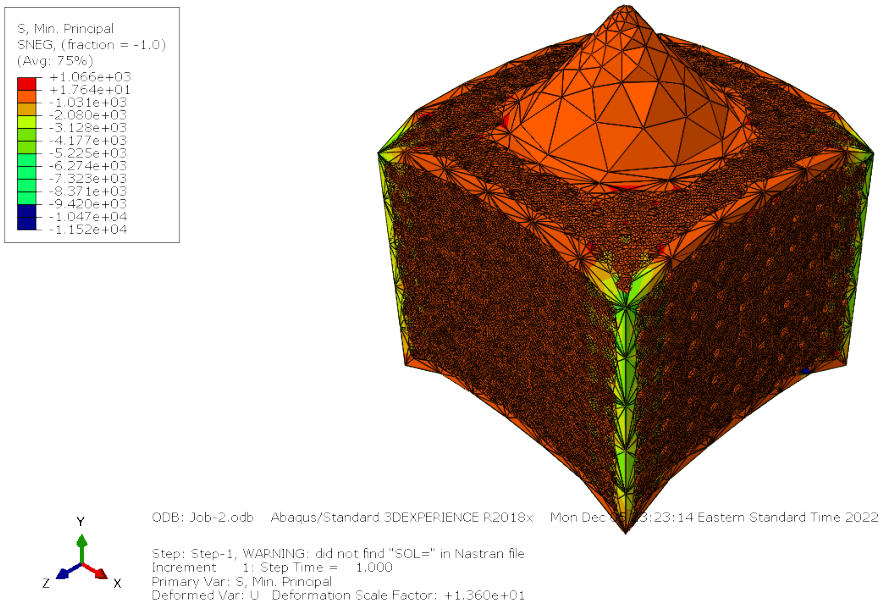

Figure 38: Min Principal Stress Results from 30 G Load in +Z Direction on Sphere Emitter Model

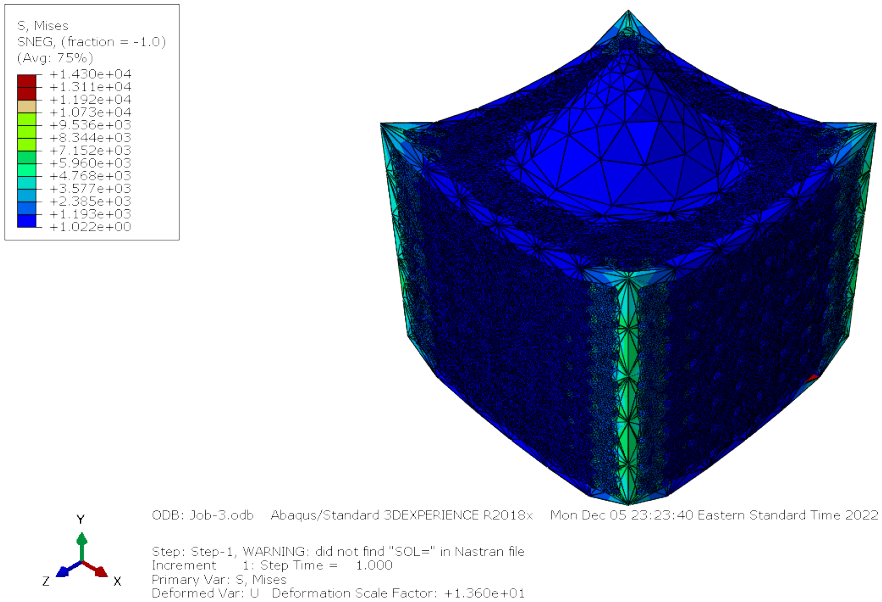

Figure 39: Von Mises Results from 30 G Load in -Z Direction on Sphere Emitter Model

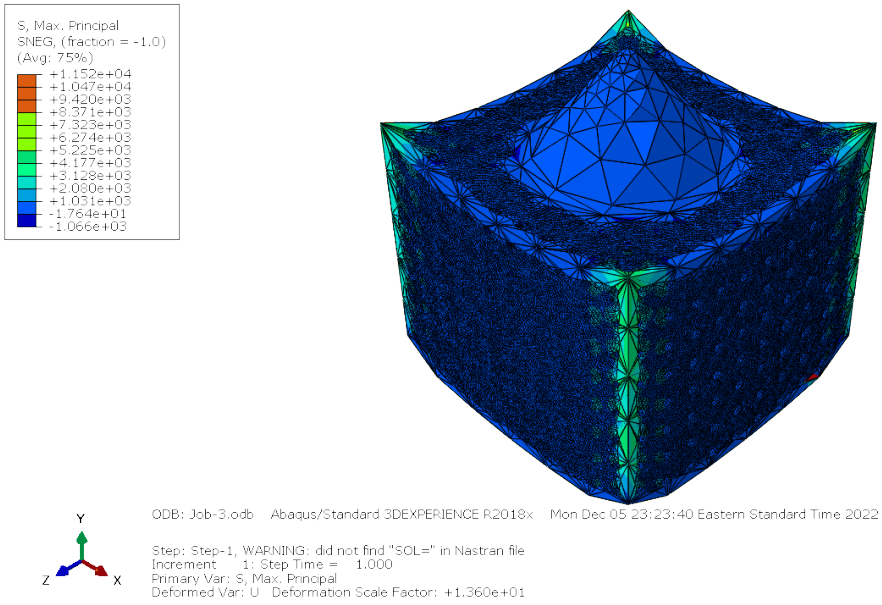

Figure 40: Max Principal Stress Results from 30 G Load in -Z Direction on Sphere Emitter Model

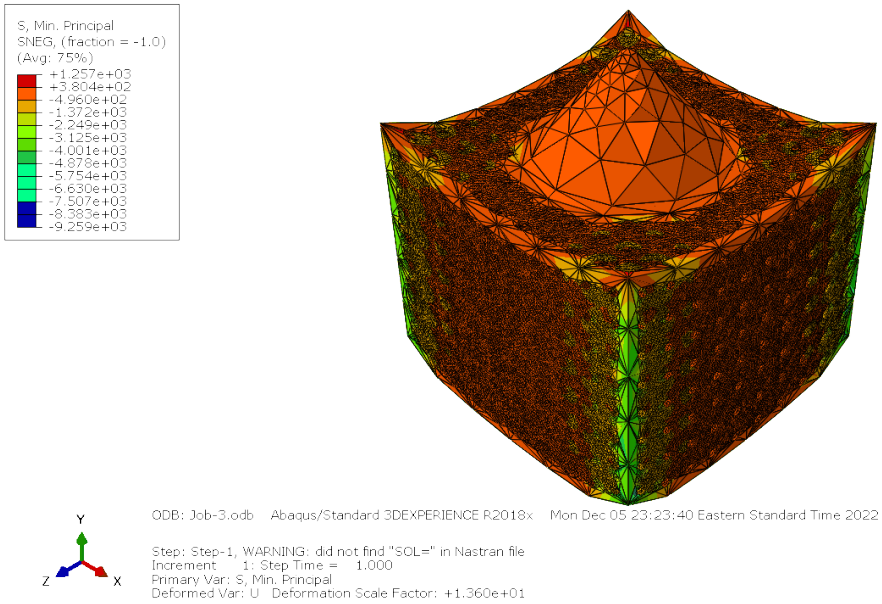

Figure 41: Min Principal Stress Results from 30 G Load in -Z Direction on Sphere Emitter Model

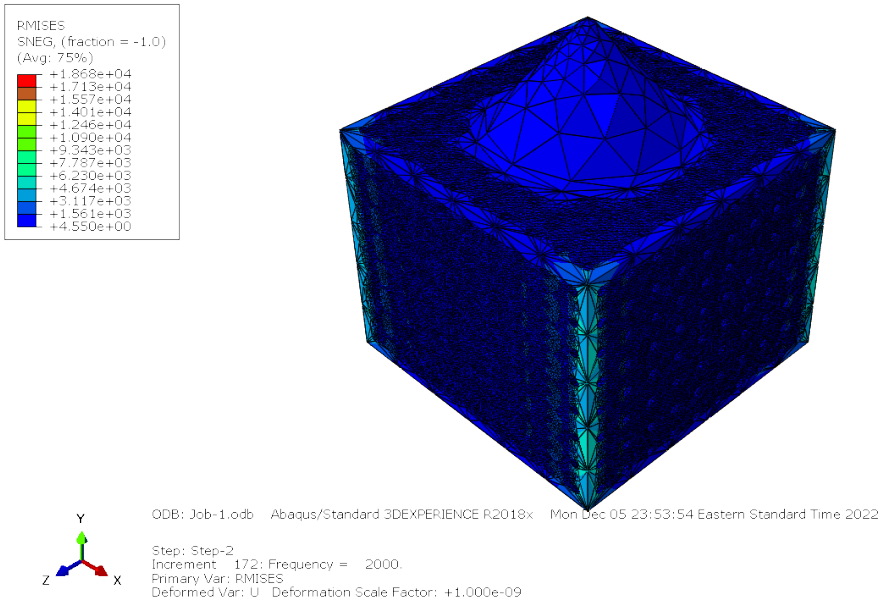

Figure 42: Root Mean Squared Von Mises Stress Results from Random Vibe on Sphere Emitter Model

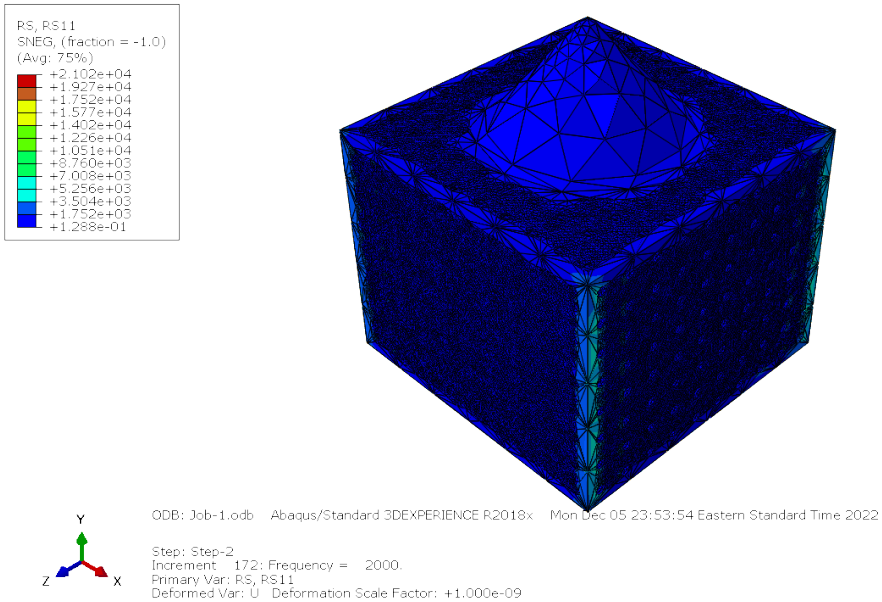

Figure 43: Root Mean Squared Stress Results from Random Vibe on Sphere Emitter Model

A.3 Diamond Model

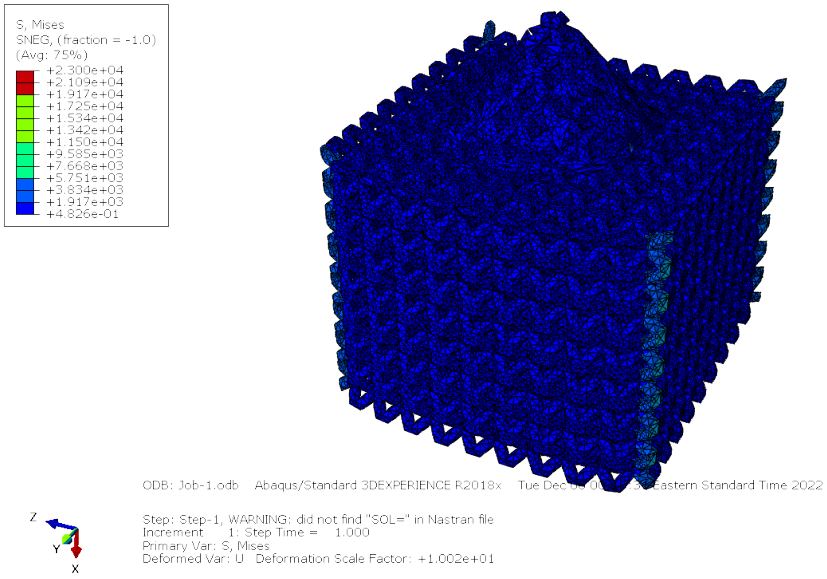

Figure 44: Von Mises Results from 30 G Load in X Direction on Diamond Emitter Model

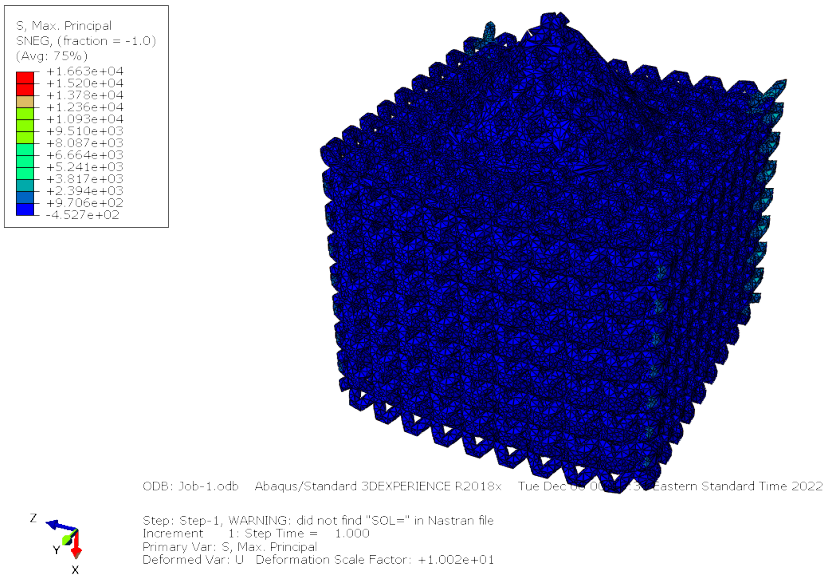

Figure 45: Max Principal Stress Results from 30 G Load in X Direction on Diamond Emitter Model

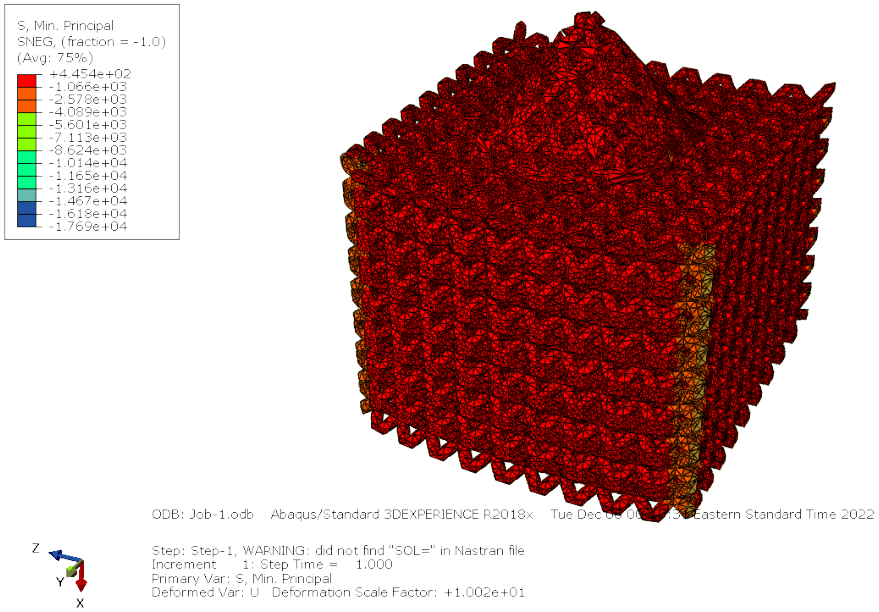

Figure 46: Min Principal Stress Results from 30 G Load in X Direction on Diamond Emitter Model

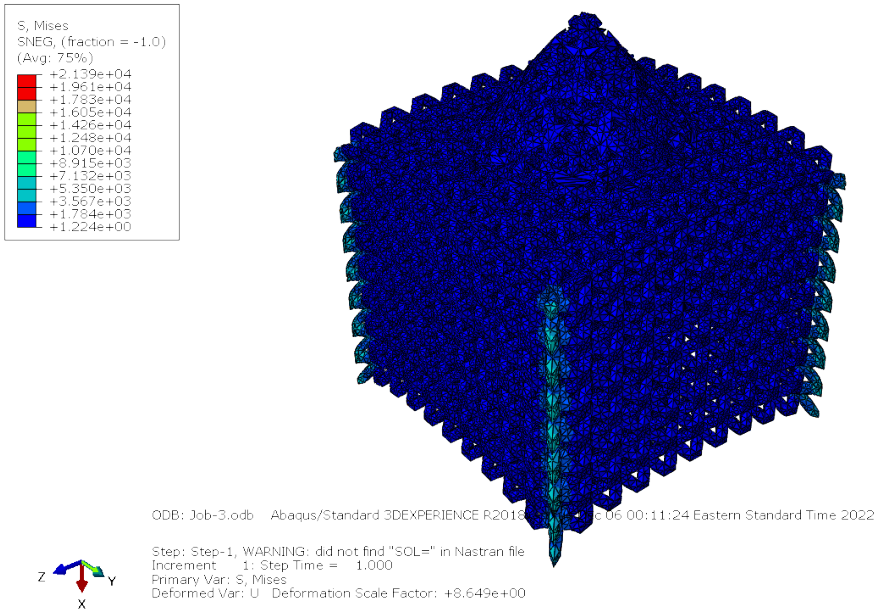

Figure 47: Von Mises Results from 30 G Load in +Z Direction on Diamond Emitter Model

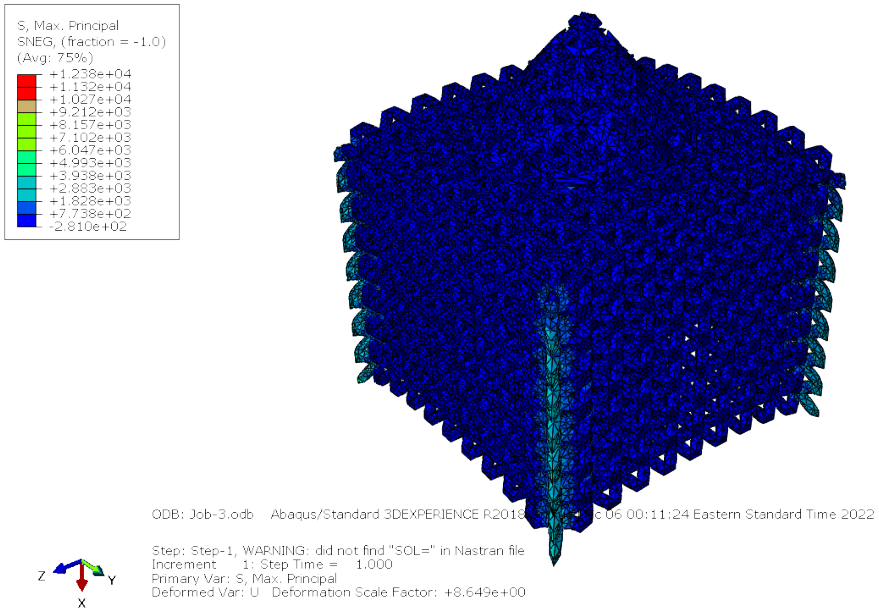

Figure 48: Max Principal Stress Results from 30 G Load in +Z Direction on Diamond Emitter Model

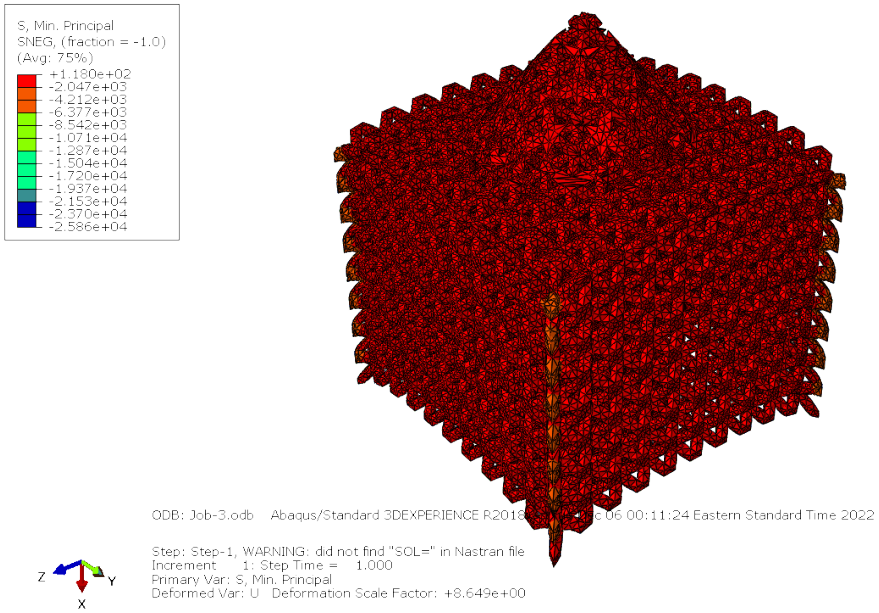

Figure 49: Min Principal Stress Results from 30 G Load in +Z Direction on Diamond Emitter Model

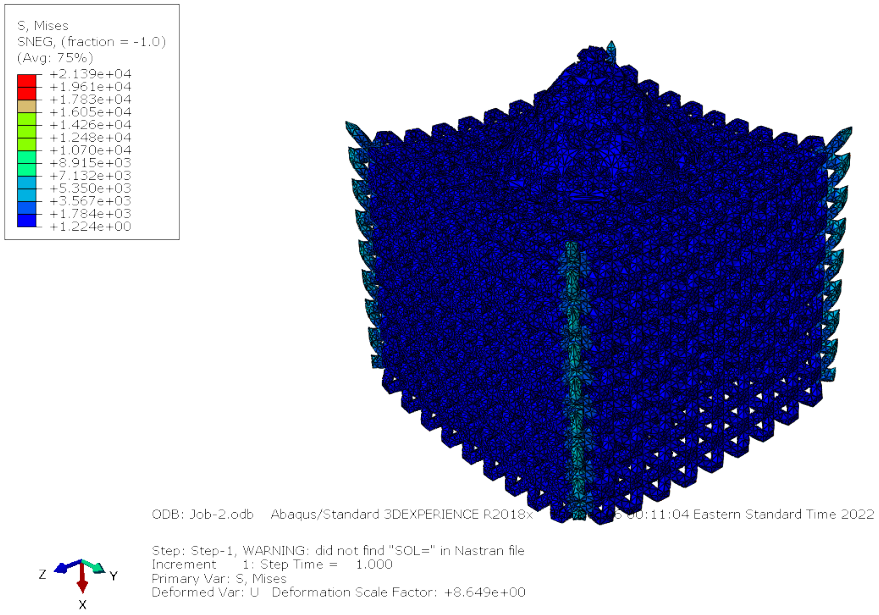

Figure 50: Von Mises Results from 30 G Load in -Z Direction on Diamond Emitter Model

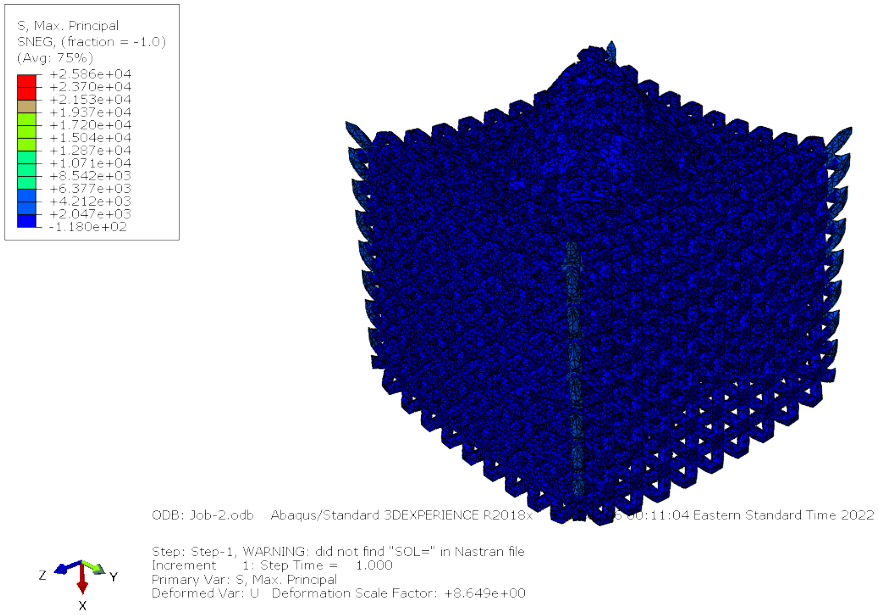

Figure 51: Max Principal Stress Results from 30 G Load in -Z Direction on Diamond Emitter Model

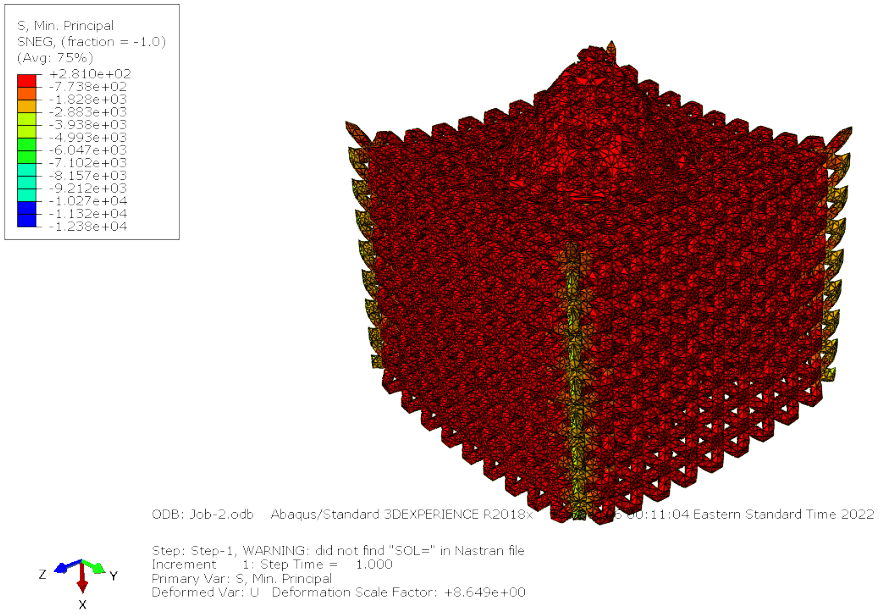

Figure 52: Min Principal Stress Results from 30 G Load in -Z Direction on Diamond Emitter Model

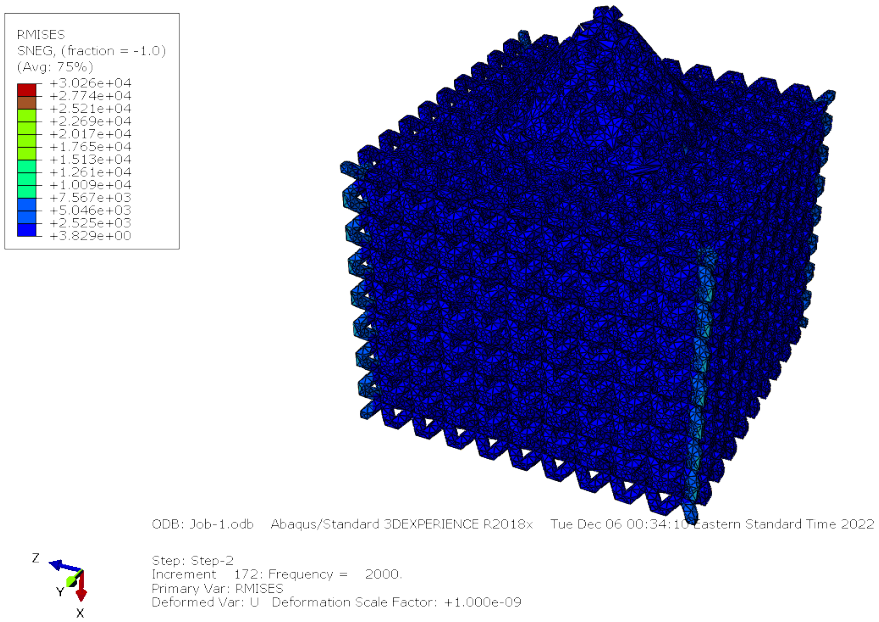

Figure 53: Root Mean Squared Von Mises Stress Results from Random Vibe on Diamond Emitter Model

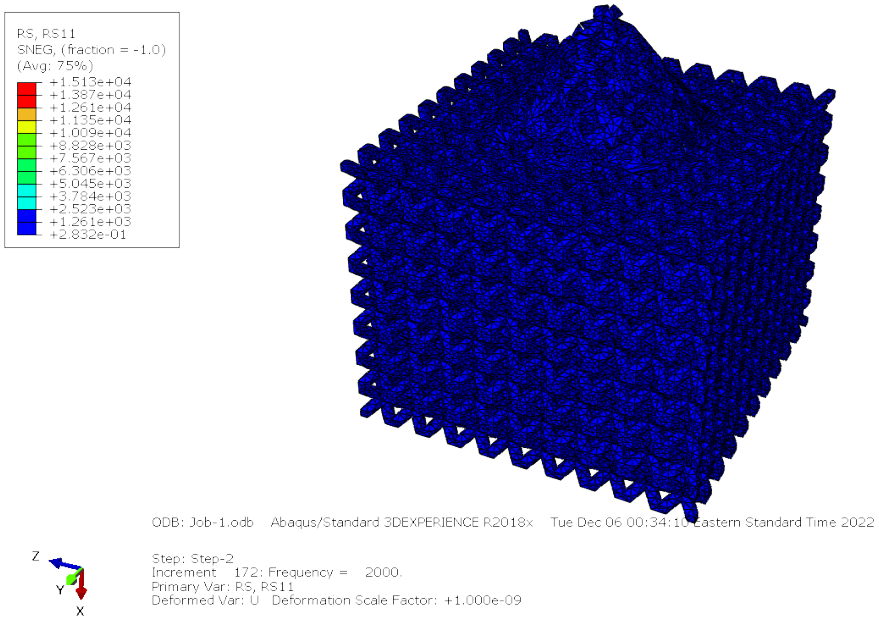

Figure 54: Root Mean Squared Stress Results from Random Vibe on Diamond Emitter Model

A.4 Body Centered Cubic Model

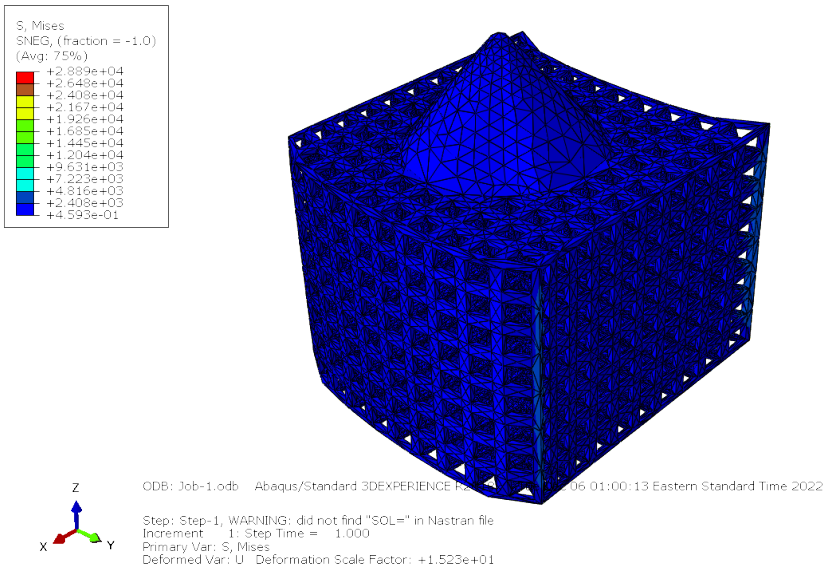

Figure 55: Von Mises Results from 30 G Load in X Direction on BCC Emitter Model

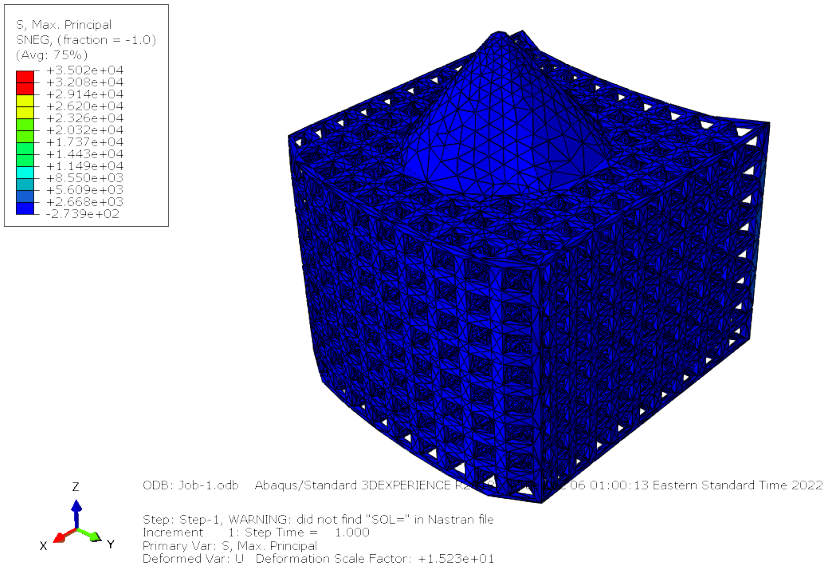

Figure 56: Max Principal Stress Results from 30 G Load in X Direction on BCC Emitter Model

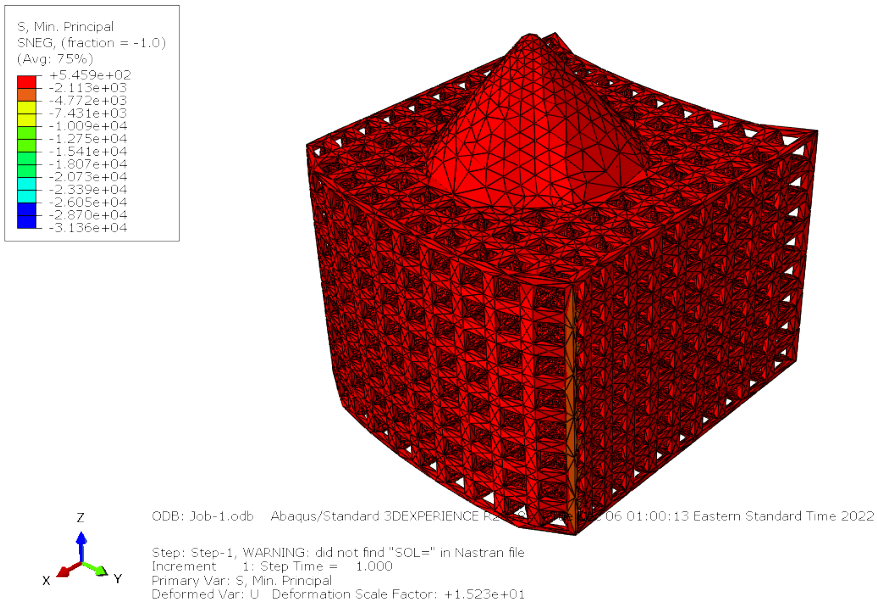

Figure 57: Min Principal Stress Results from 30 G Load in X Direction on BCC Emitter Model

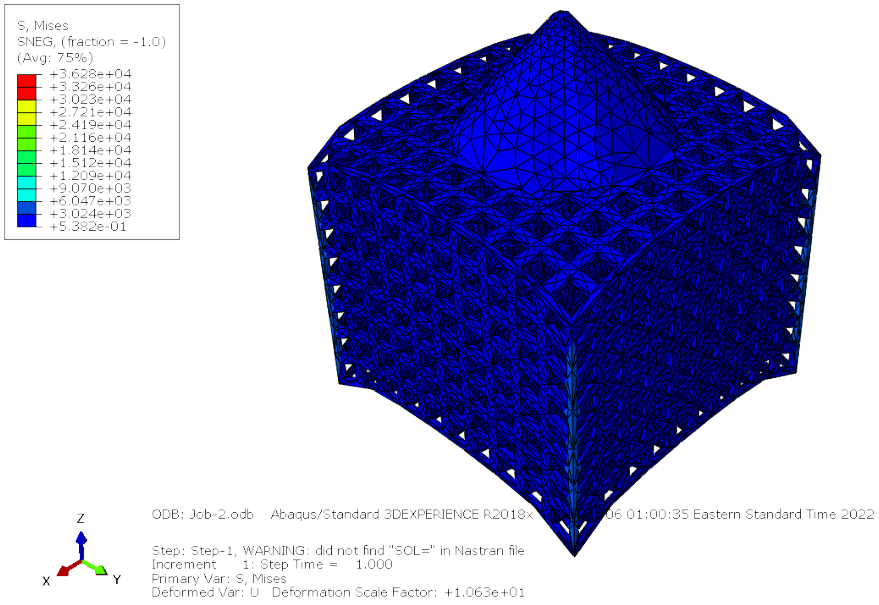

Figure 58: Von Mises Results from 30 G Load in +Z Direction on BCC Emitter Model

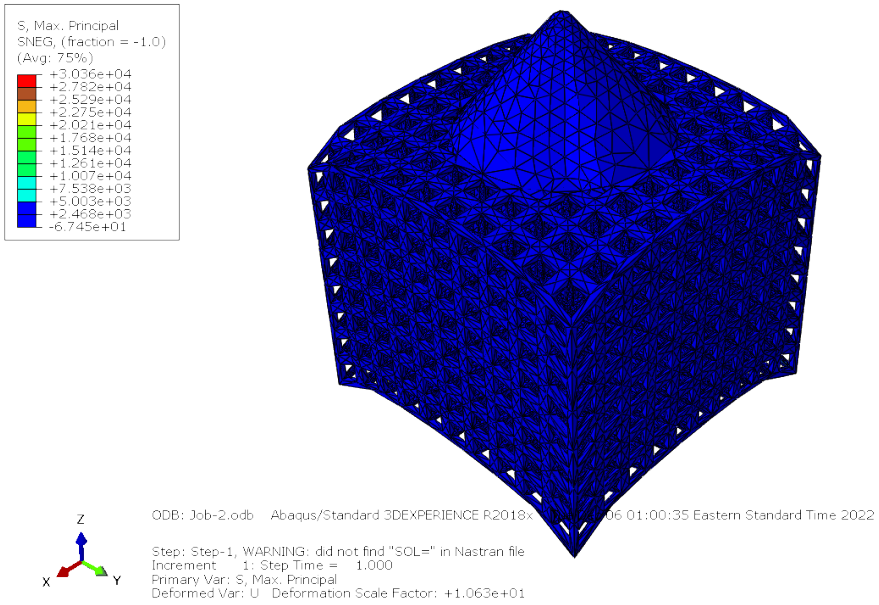

Figure 59: Max Principal Stress Results from 30 G Load in +Z Direction on BCC Emitter Model

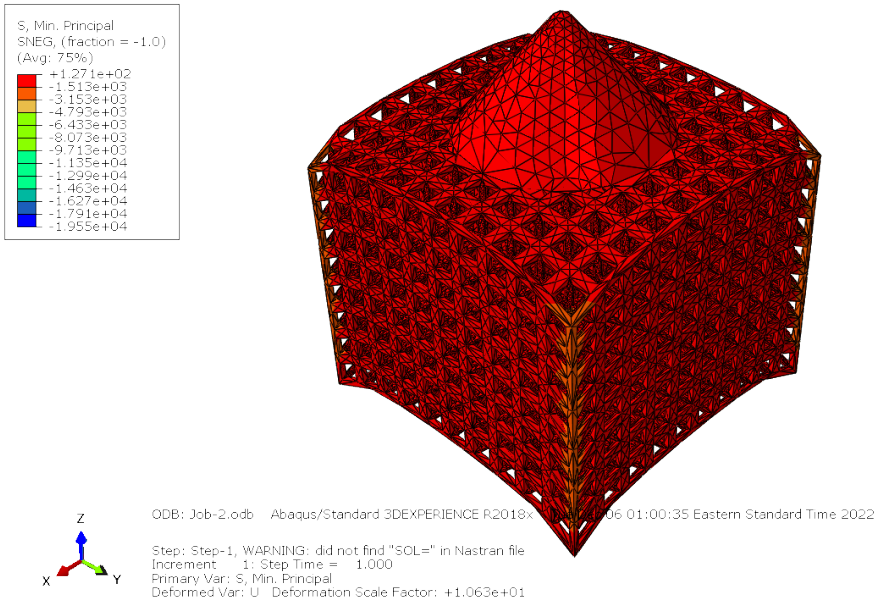

Figure 60: Min Principal Stress Results from 30 G Load in +Z Direction on BCC Emitter Model

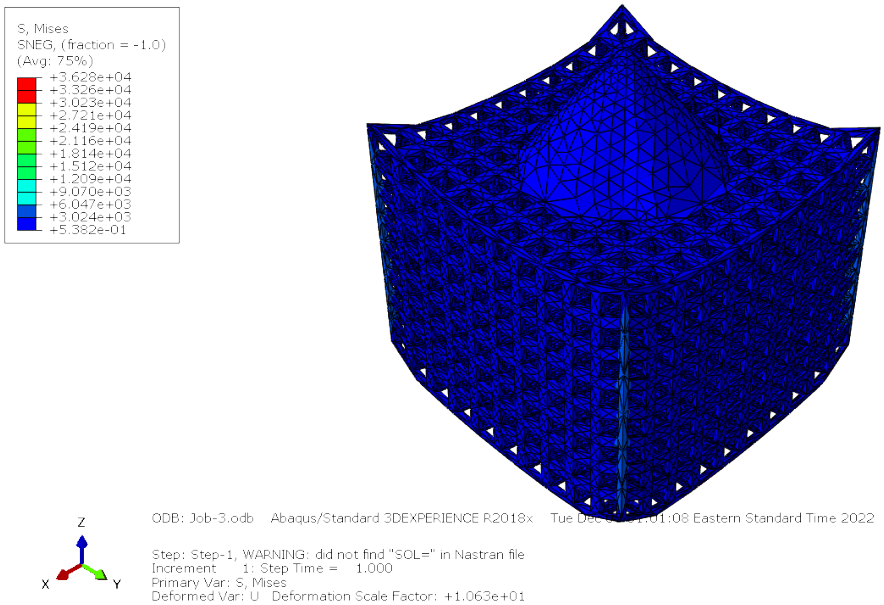

Figure 61: Von Mises Results from 30 G Load in -Z Direction on BCC Emitter Model

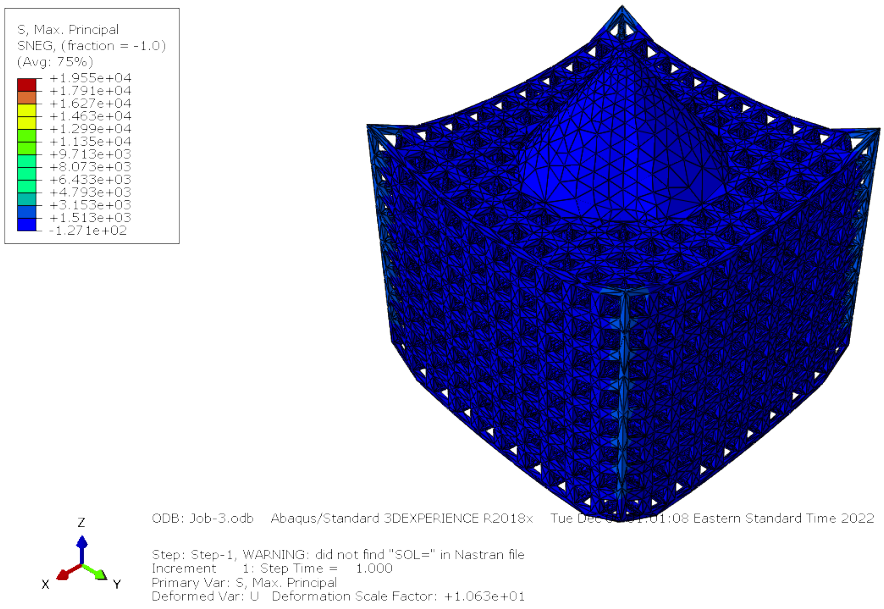

Figure 62: Max Principal Stress Results from 30 G Load in -Z Direction on BCC Emitter Model

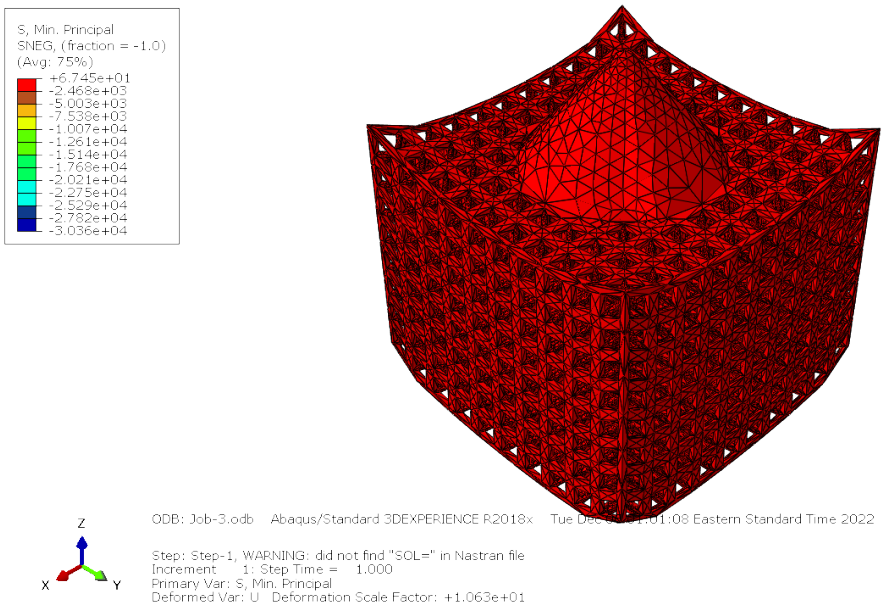

Figure 63: Min Principal Stress Results from 30 G Load in -Z Direction on BCC Emitter Model

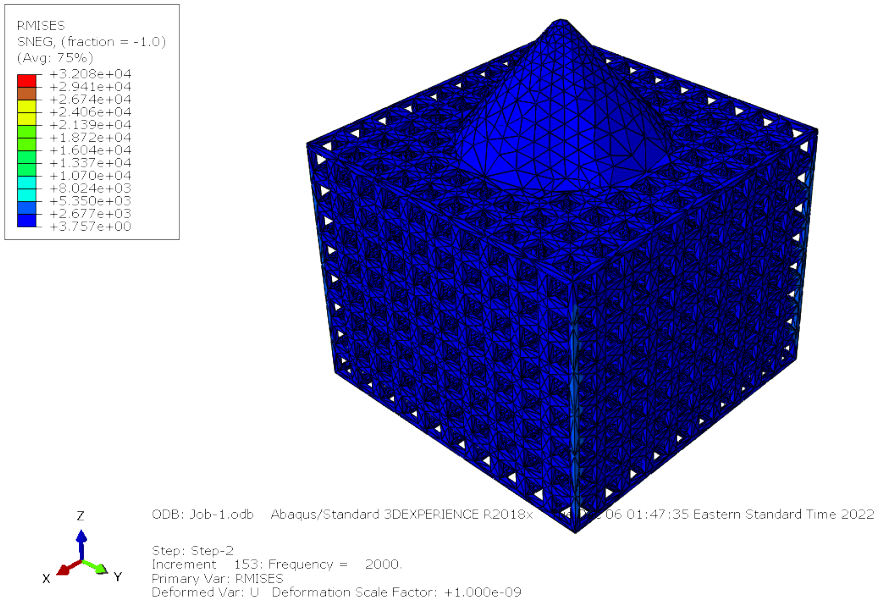

Figure 64: Root Mean Squared Von Mises Stress Results from Random Vibe on BCC Emitter Model

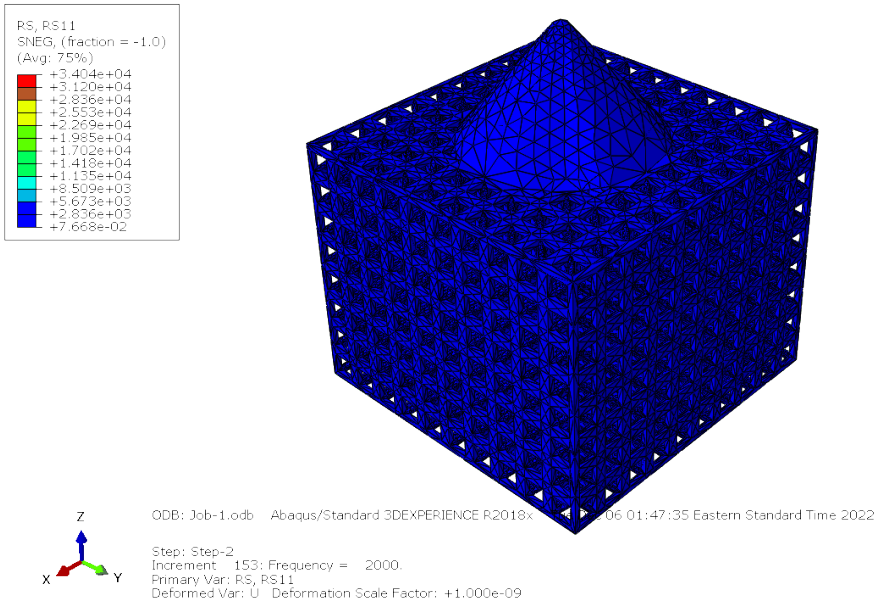

Figure 65: Root Mean Squared Stress Results from Random Vibe on BCC Emitter Model